JOURNAL OF GEOPHYSICAL RESEARCH, VOL. 113, A06303, doi:10.1029/2007JA012693, 2008

Excitation of ducted gravity waves in the lower thermosphere by tropospheric sources

Jonathan B. Snively[1,2] and Victor P. Pasko[1]

Received 29 July 2007; accepted 11 January 2008; published 5 June 2008.

[1] Short-period, small-scale gravity waves are frequently observed in nighttime airglow imaging experiments. These waves are often found to be ducted and may be confined to a thin region of altitude in the mesosphere or lower thermosphere. An apparent paradox of high-altitude ducted waves is the nature of the source; it is necessary that a ducted wave be excited in situ or have been able to tunnel into the duct from another atmospheric region. In this paper, analytical and numerical solutions are presented for simple thermally ducted gravity waves that are Doppler-shifted by constant background winds. Using a continuous analytical model, duct dispersion properties are calculated for three case studies. Using a fully nonlinear numerical model, several scenarios are explored by which a tropospheric source can excite these thermally ducted wave modes. First, we validate the analytical and numerical models for the classical case of linear wave tunneling. Second, we examine the nonlinear excitation of ducted waves due to resonant wave self-interactions associated with realistic propagation and small-scale wavebreaking, for propagation in the same direction as the wind flow. Third, we consider the case of ducted wave excitation and propagation opposite to the direction to wind flow. Specifically, where horizontal group and phase velocities exhibit opposite sign in the ground-relative frame. The results suggest that ducted waves of very short period can be excited in the lower thermosphere by tropospheric sources, via simple linear and nonlinear processes. These excitation mechanisms are likely to be robust for a range of realistic thermal and thermal-Doppler ducts.

Citation: Snively, J. B., and V. P. Pasko (2008), Excitation of ducted gravity waves in the lower thermosphere by tropospheric sources, *J. Geophys. Res.*, *113*, A06303, doi:10.1029/2007JA012693.

1. Introduction

[2] There is strong theoretical and observational evidence that thunderstorms represent significant sources of short-period, small-scale gravity wave activity throughout the middle and upper atmosphere [e.g., *Fritts and Alexander*, 2003, and references therein]. Mechanical oscillations of air due to penetrative convection at thundercloud tops are believed to be a dominant forcing mechanism of small-scale gravity waves [e.g., *Pierce and Coroniti*, 1966; *Stull*, 1976; *Fovell et al.*, 1992]. This process has been simulated in numerous modeling studies for squall-line and isolated convective sources [e.g., *Alexander et al.*, 1995; *Piani et al.*, 2000; *Horinouchi et al.*, 2002]. Evidence of thunderstorm-generated waves includes rocket observations of mesospheric heating above thunderstorms [*Taylor*, 1979], and radar detection of upward traveling gravity waves at stratospheric altitudes above thunderstorms [*Larsen et al.*, 1982]. Ground-based [*Taylor and Hapgood*, 1988; *Sentman et al.*, 2003] and satellite-based [*Dewan et al.*, 1998] observations of stratospheric and mesospheric nightglow emissions have also revealed coherent circular gravity wave structure, clearly associated with underlying thunderstorm activity.

[3] Airglow imaging studies have confirmed that quasi-monochromatic, small-scale, gravity waves frequently propagate through the mesosphere and lower thermosphere. Waves with short periods of $5 \leq \tau \leq 8$ min and horizontal wavelengths (λ_x) on the order of a few tens of kilometers are often observed [e.g., *Taylor et al.*, 1995; *Nakamura et al.*, 1999; *Walterscheid et al.*, 1999; *Hecht et al.*, 2001; *Chung et al.*, 2003]. These include both short-period "band" structures and localized "ripple" structures with periods near or below the Brunt-Väisälä period of 5 min. Quasi-monochromatic, short-period "band" structures may be indicative of propagating, ducted, or evanescent waves while many of the "ripple" events may be indicative of short-lived shear instability structures [e.g., *Horinouchi et al.*, 2002; *Hecht*, 2004, and references therein].

[4] It has been suggested that many of the short-period waves observed in airglow data may be guided or trapped by a thermal duct [e.g., *Walterscheid et al.*, 1999, 2001] or Doppler duct [e.g., *Isler et al.*, 1997], where propagation is confined to a fixed altitude region by the atmospheric thermal or wind structure, respectively. Because they are

[1]Communications and Space Sciences Laboratory, Department of Electrical Engineering, Pennsylvania State University, University Park, Pennsylvania, USA.
[2]Now at Center for Atmospheric and Space Sciences, Utah State University, Logan, Utah, USA.

0148-0227/08/2007JA012693$09.00

vertically confined and exhibit relatively minimal propagation loss, ducted waves can travel great horizontal distances, as long as the atmospheric structure remains reasonably consistent. Consequently, ducted waves are able to influence regions of the atmosphere far from the source.

[5] An obstacle to the excitation of ducted waves at airglow altitudes is the region of evanescence forming the lower boundary of the duct. Short-period wave energy, which may otherwise be ducted, will be subject to evanescence and downward reflection as it propagates upward into the lower duct boundary. However, without this lower bounding region, the duct would cease to exist. Excitation of lower-thermospherically ducted waves requires that wave energy be able to tunnel through this boundary [e.g., *Sutherland and Yewchuk*, 2004, and references therein] or for ducted waves to be excited in situ. *Taylor and Edwards* [1991] observed ducted gravity waves at airglow altitudes with periods near 5 min and proposed that the wave source would likely have been in situ, due to these challenges.

[6] For tunneling to occur, it is implicit that there exist a duct at lower altitude in which wave energy can be initially trapped. Where modal dispersion curves of two vertically adjacent ducts overlap, ''kissing'' (Eckart's resonance) between modes occurs [*Jones*, 1970; *Fritts and Yuan*, 1989]. Energy can be exchanged most effectively at these points, as one ducted mode can transfer energy to another ducted mode at the same frequency and horizontal wave number. This simple coupling mechanism provides an effective linear means for a short-period, tropospherically generated gravity wave to become ducted at altitudes above mesopause [*Jones*, 1970; *Fritts and Yuan*, 1989; *Walterscheid et al.*, 2001; *Sutherland and Yewchuk*, 2004]. These exchanges can also occur for nonideally ducted wave packets, albeit with greater propagation losses [e.g., *Yu and Hickey*, 2007].

[7] Using a cylindrically symmetric, two-dimensional numerical model, *Walterscheid et al.* [2001] applied a convective source at tropospheric altitudes to study the generation and propagation of short period gravity waves in a thermally realistic, windless atmosphere. Results clearly indicated coupling between two atmospheric ducts, where a wave packet first propagates into a stratospheric duct before transferring a part of its energy vertically into the lower thermospheric duct. In all simulation results presented by *Walterscheid et al.* [2001], ducted small-scale waves were excited in the lower thermosphere with periods near 6 min. These simulated waves were consistent with past observations of small-scale gravity waves [e.g., *Walterscheid et al.*, 1999; *Hecht et al.*, 2001]. The interaction between ducts in this case resembles that associated with the ''kissing'' modes described in past studies [e.g., *Fritts and Yuan*, 1989].

[8] This duct coupling mechanism modeled by *Fritts and Yuan* [1989] and *Walterscheid et al.* [2001] is valid only when the gravity waves are of linear magnitude at all altitudes. Owing to the exponential decrease of density with altitude, the velocity perturbation associated with a gravity wave must increase exponentially to conserve kinetic energy with altitude [e.g., *Gossard and Hooke*, 1975, p. 76–77]. Thus, gravity waves grow significantly in magnitude as they propagate vertically. It can be expected that many of these waves will break, or attain magnitudes sufficient for nonlinear behavior, at some altitude near or above the mesopause. This is particularly a concern for strong squall line sources, where wave magnitude does not strongly decrease with radial distance from the source [e.g., *Alexander et al.*, 1995].

[9] *Chimonas et al.* [1996] outlined a simple nonlinear mechanism by which a vertically propagating gravity wave can excite ducted waves in situ, as it passes through an atmosphere of varying wind or thermal structure. As the wave passes through a potential ducting region, it interacts with itself through a nonlinear wave triad resonance. This wave interaction is equivalent to the interaction of two waves with frequency ω and wave number k_x and results in the transfer of energy from the primary wave to a new ducted secondary wave with frequency 2ω and wave number $2k_x$.

[10] Similar wave-wave interactions have been found to occur during wave breaking. Recent nonlinear studies of wave breaking in two dimensions have demonstrated that coherent secondary waves can be excited in the region of breaking [e.g., *Andreassen et al.*, 1994; *Franke and Robinson*, 1999]. In particular, *Franke and Robinson* [1999] demonstrated the excitation of both acoustic and gravity waves during the breaking of short-period gravity waves in a periodic and isothermal simulation domain. The excitation mechanism was explained in terms of a nonlinear wave-wave interaction of the primary wave, the interaction product being the observed harmonic secondary waves. The secondary waves had characteristic frequencies and horizontal wave numbers that were integer multiples of the source waves, with wave perturbation magnitudes consecutively weaker for each higher mode. The periodic domains used by *Andreassen et al.* [1994] and *Franke and Robinson* [1999], however, ensure that exact harmonics of the domain width (and horizontal wavelength) will be preferentially excited. Furthermore, interactions during wave breaking in a periodic domain are enhanced, since faster portions of the packet spectrum cannot propagate horizontally away from the breaking region.

[11] *Satomura and Sato* [1999] studied the breaking of mountain waves as a source of secondary gravity waves in the lower atmosphere and demonstrated that the secondary waves could become ducted by the thermal and wind structure of the stratosphere. *Zhou et al.* [2002] studied the generation of secondary waves for breaking of a broadband packet; generated waves were attributed to convection arising from the breaking process. As a means to model the effects of breaking, *Vadas et al.* [2003] treated the generation of secondary waves as a linear forced response to the small-scale convection in the breaking region. *Vadas et al.* [2003] noted that these secondary waves may become ducted if the breaking region is located near or inside a duct. This proposed mechanism differs from that of *Franke and Robinson* [1999] and assumes a linear convective forcing response rather than nonlinear wave resonance.

[12] *Snively and Pasko* [2003] presented a numerical experiment demonstrating the nonlinear excitation of short period ducted waves in the lower thermopshere. Primary waves of $\sim$10 min were excited by a tropospheric oscillatory source and allowed to propagate vertically to the point of breaking in the lower thermosphere. Simultaneous to the onset of primary wave breaking, short-period secondary waves with periods $\sim$5 min were radiated downward into the lower thermospheric duct, where they were captured. These harmonic waves arise principally from wave self-

interactions [e.g., *Chimonas et al.*, 1996; *Franke and Robinson 1999*].

[13] A strong short-period gravity wave event was recently reported by *Smith et al.* [2006], where a wave of ~8 min ground-relative period was observed to propagate simultaneously with a ~16 min wave, with wavelengths ~20 km and ~35 km, respectively, and both exhibiting comparable phase velocity. It was calculated that the intrinsic period of the smaller-scale wave was ~5 min, consistent with ducted wave periods. The observed frequencies, wavelengths, and phase velocities suggest a nonlinear origin for the smaller-scale wave, perhaps as a harmonic of the larger wave. Curvature of the wave fronts was also noted, suggesting that the event may have been observed near to its original source location, at a distance of ~90–180 km depending on intervening wind flow. However, no candidate tropospheric sources were identified.

[14] Another notable example of a ducted short-period wave was reported by *Taylor et al.* [1995], which exhibited several distinct features. The observed wave had a ground-relative period τ = 4.4 min and horizontal wavelength λ_x = 20 km. Additional similar wave events have since been reported [e.g., *Smith et al.*, 2003, 2005; *Brown et al.*, 2004; *Snively et al.*, 2007]. These events are consistent with waves near the ducted/evanescent limit of propagation, with typical periods of $\tau \sim 5$ minutes and horizontal wavelengths $\lambda_x \sim$ 20 km. These events also appear front-like, exhibiting distinct background enhancements or depletions of airglow intensity, which are phase-locked with the leading edge of the short-period wave. An explanation proposed by *Dewan and Picard* [1998, 2002] attributes this background intensity jump to a larger-scale dynamic perturbation, which is believed to be forcing the short-period waves. Such "mesospheric bores," analogous to shallow water bores, would consist of strong large-scale fluid motions forcing ducted internal gravity waves [e.g., *Seyler*, 2005], providing an additional in situ generation mechanism for ducted waves at mesopause altitudes. The associated modal structure and dispersion properties, however, satisfy gravity wave ducting theory. For example, it has been proposed by *Munasinghe et al.* [1998] and demonstrated by *Snively and Pasko* [2005], and in this paper, that a ducted gravity wave mode does exist, which closely matches the properties of the wave reported by *Taylor et al.* [1995].

[15] There are two primary goals of this paper: First, we will outline a new two-dimensional numerical model for gravity wave propagation in a realistic atmosphere, spanning the altitude range from ground to the lower thermosphere. Second, we will explore the excitation of thermally ducted waves in the lower thermosphere by tropospheric sources, presenting three sets of simulation results. Analytical ducted mode solutions are used to choose parameters for the model studies and are presented for the sake of comparison and validation. These simulated case studies are as follows:

[16] 1. (I-Validation) We explore the linear problem of "kissing" modes and wave tunneling between stratospheric and lower thermospheric ducts in a windless atmosphere. Numerical model results will be validated against a continuous analytic duct model and previous numerical studies [*Walterscheid et al.*, 2001].

[17] 2. (IIa,b) We examine the ducted wave excitation mechanism discussed by *Snively and Pasko* [2003] for a model atmosphere with a constant background wind present in the wave ducting regions. Under these conditions, we explore secondary wave excitation for cases where a primary wave of focused spectrum breaks just above the duct [e.g., *Snively and Pasko*, 2003] with fixed (IIa) and broad (IIb) source wave number spectra. These cases occur where resulting ducted wave packet propagates with horizontal group and phase velocity in the direction of the wind flow (downwind), under conditions described by *Snively and Pasko* [2005] based on the event reported by *Taylor et al.* [1995]. Details of the analytical solutions verifying the existence of this ducted wave mode, along with excitation of this wave mode, were omitted from [*Snively and Pasko*, 2005] and are presented and discussed here.

[18] 3. (III) We consider the case where the ducted wave propagates against the wind flow inside the duct (upwind). The wind flow shifts the intrinsic frequency higher, allowing waves with longer ground relative periods to satisfy thermally ducted mode solutions. In this particular case, the wave is Doppler-shifted such that horizontal phase and group velocity exhibit opposite sign in the ground-relative frame.

2. Analytical Theory of Ducting

[19] Short-period gravity wave propagation strongly depends on the preexisting temperature and wind structure of the atmosphere. In an isothermal, windless atmosphere, a freely propagating internal gravity wave packet could travel vertically until the point of instability and breaking [e.g., *Hines*, 1960]. In a physical atmosphere, with wind and thermal variations, gravity waves can be reflected prior to breaking or become ducted between reflective layers in which the wave becomes evanescent. Ideally ducted waves may be described mathematically by bounded wave solutions, and satisfy discrete modal dispersion curves [e.g., *Gossard and Hooke*, 1975, pp. 150–165]. Here we review the properties of a simple analytical gravity wave duct.

2.1. General Duct Properties

[20] Vertical wave structure in a constant background flow can be described approximately under the Boussinesq approximation for an incompressible atmosphere using a simplified version of the Taylor-Goldstein equation, which describes the normalized vertical perturbation velocity w_z [e.g., *Gossard and Hooke*, 1975, pp. 123–124]:

$$\frac{\partial w_z^2}{\partial z^2} + k_z^2 w_z = 0 \tag{1}$$

$$k_z^2 = \frac{N^2}{(U - \omega/k_x)^2} - k_x^2 \tag{2}$$

[21] By examining a profile of vertical wave number squared (k_z^2) for given wave frequency (ω), mean horizontal wind velocity (U), horizontal wave number (k_x), and Brunt-Väisälä frequency squared profile (N^2) [*Isler et al.*, 1997] duct boundaries can be inferred.

[22] Where $k_z^2>0$, waves characterized by corresponding ω and k_x are able to propagate, where $k_z^2<0$ indicates

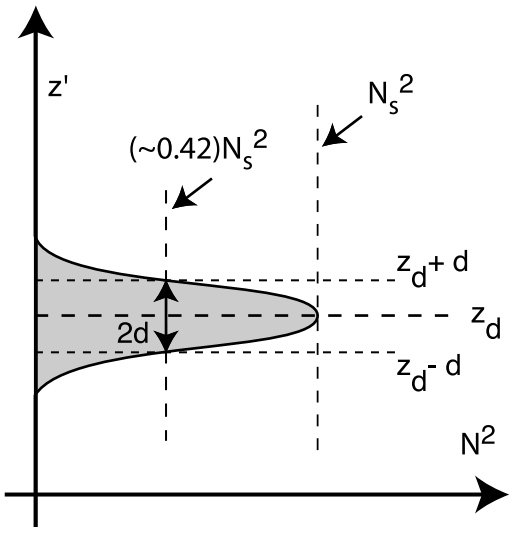

Figure 1. Continuous model profile of Brunt-Väisälä frequency supporting ducted wave propagation.

evanescence. A region of the atmosphere where k_z^2 is positive and confined above and below by regions of negative k_z^2, will form a duct for waves of ω and k_x. This ducting is only ideal, however, if an integer number of vertical half wavelengths are able to effectively fit within the boundaries. For pure thermal ducting with zero mean flow, wave ducting occurs in the same manner for propagation in any horizontal direction. Where horizontal flow becomes significant, but without shear, the duct will impose ground-relative directionality constraints in accordance with the associated Doppler shift.

2.2. Linear Continuous Duct Model

[23] While it is possible to solve a boundary value problem for a layered system supporting simple ducted wave modes, a continuous buoyancy profile will more closely predict the modal dispersion properties of a physical atmospheric duct. Unlike our numerical model, the continuous analytical model discussed here does not provide for nonideal ducting, but it allows estimation of ideal ducted mode dispersion properties. These ideal dispersion curves will be used to confirm existence of wave solutions and to choose focused source parameters for our model case studies.

[24] The model which we will use was originally outlined by *Groen* [1948], and revisited by *Thorpe* [1968] and *Gossard and Hooke* [1975, pp. 162–165]. Although our numerical model (outlined in section 3) includes the effects of compressibility, at the phase velocities of interest the motions will be approximately consistent with those of an incompressible system. The analytical model therefore works under the incompressible Boussinesq approximation. The derivation, which was originally presented for an oceanic thermocline internal wave duct, assumes a stable density profile:

$$\rho_o(z) = \rho_s[1 - (\Delta\rho/\rho_s)\tanh(z/d)] \tag{3}$$

[25] The density varies by $\pm\Delta\rho$ from the average value at $\rho_o(0) = \rho_s$, approaching its maximum as $z \rightarrow -\infty$ and minimum as $z \rightarrow +\infty$. For an incompressible system, $N^2 = -(g/\rho_o)(d\rho_o/dz)$ [e.g., *Gossard and Hooke*, 1975, p. 73], and it can be found that

$$N^2 = N_s^2 \cosh^{-2}(z/d) \tag{4}$$

where $N_s = g\Delta\rho/\rho_s d$. In the atmosphere it is conventional to express the Brunt-Väisälä frequency in terms of potential temperature rather than density. In this case, $N^2 = (g/\theta_o)(d\theta_o/dz)$, where θ_o is potential temperature [e.g., *Gossard and Hooke*, 1975, pp. 71–75]. Therefore,

$$\theta_o(z) = -\theta_s[1 - (\Delta\theta/\theta_s)\tanh(z/d)] \tag{5}$$

where θ_s is arbitrary and $\Delta\theta = N_s\theta_s d/g_o$. The equation (5) is equivalent to equation (3), however with potential temperature varying by $\pm\Delta\theta$ from the average value at $\theta_o(0) = \theta_s$, approaching it's maximum as $z \rightarrow -\infty$ and minimum as $z \rightarrow +\infty$.

[26] The Brunt-Väisälä (N^2) profile specified by equation (4) is shown schematically in Figure 1 for a duct positioned at an arbitrary height z_d, where the substitution $z = z' - z_d$ has been made to place the duct at some altitude far above ground.

[27] The wave equation (1) for the selected N^2 profile can be written in the form:

$$\frac{\partial^2 w_z}{\partial z^2} + \left[k_x^2 + \frac{N_s^2 k_x^2}{\hat{\omega}^2}\cosh^{-2}(z/d)\right] w_z = 0 \tag{6}$$

where $\hat{\omega} = \omega - k_x U$ is the intrinsic frequency, and U represents the constant ambient wind velocity. A general solution of this equation may be obtained in terms of Gauss hypergeometric functions. The modal solutions for w_{zm} for a duct located at z_d can then be expressed approximately for each mode m in terms of hyperbolic trigonometric functions [e.g., *Thorpe*, 1968; *Gossard and Hooke*, 1975, pp. 163–164]. The dispersion properties of each mode m are described by the dispersion relation [*Gossard and Hooke*, 1975, p. 164]:

$$\hat{\omega}^2 = \frac{k_x^2 N_s^2 d^2}{[(k_x d + m - 1)(k_x d + m)]} \tag{7}$$

[28] By assuming a fixed horizontal wave number k_x or intrinsic frequency $\hat{\omega}$, the vertical structure of a ducted wave mode can be predicted. These waves do not have a characteristic vertical wave number, as they exhibit complex vertical structure with $p = m$-1 nodes, and approach sinusoidal solutions as p becomes large. Our case study analytical solutions described in sections 4.1 and 5.1 are determined approximately, by first fitting an analytical duct N^2 profile to the physical N^2 profile, to closely match the real system over the frequency range of interest.

[29] The modal dispersion relation for the ground-relative frequency can be written as follows:

$$\omega = k_x U + \sqrt{\frac{k_x^2 N_s^2 d^2}{[(k_x d + m - 1)(k_x d + m)]}} \tag{8}$$

[30] The ground-relative horizontal phase velocity (ω/k_x) is

$$v_{px} = U + \sqrt{\frac{N_s^2 d^2}{[(k_x d + m - 1)(k_x d + m)]}} \tag{9}$$

[31] The ground-relative horizontal group velocity is obtained by taking $d\omega/dk_x$:

$$v_{gx} = U + \frac{1}{2}\frac{N^2 d^2 k_x (2m-1) + 2N^2 dm(m-1)}{\left(d^2 k_x^2 + 2mdk_x - dk_x + m^2 - m\right)^{3/2}} \tag{10}$$

[32] It is important to note that the analytical duct is able to support trapped modes with frequencies much lower than the physical duct. The solutions are applicable only for frequencies where the Brunt-Väisälä profiles of the analytical and physical ducts closely overlap. Furthermore, this analytical model does not permit nonideal ducting or free wave propagation.

[33] Negative ground-relative group velocity may be obtained for strong wind flow opposing the direction of intrinsic group propagation ($\hat{v}_{gx}$, where $v_{gx} = \hat{v}_{gx} + U$); i.e., if U is negative and $\hat{v}_{gx} < -U$. It is thus possible for the ground-relative group velocity and phase velocity to be in opposite directions for a horizontally propagating ducted gravity wave. A similar situation arises for a freely propagating gravity wave packet in strong wind, however here the vertical group velocity is zero due to trapping. This may also occur for Doppler-ducted waves under certain conditions [e.g., *Chimonas and Hines*, 1986]. As demonstrated later in section 5.3 for this case, wave packet energy propagates in the opposite direction of the observed phase progression. This is loosely analogous to electromagnetic wave propagation in material with negative index of refraction [e.g., *Veselago*, 1968; *Cummer*, 2003].

[34] In this subsection we have reviewed approximate analytical solutions for ducted wave modes. An alternative approach would be to obtain one-dimensional steady-state solutions numerically, by solving the Taylor-Goldstein equation for a specific set of atmospheric profiles [e.g., *Fritts and Yuan*, 1989]. However, the analytical solutions presented here agree well with previously observed and predicted wave modes [e.g., *Taylor et al.*, 1995; *Munasinghe et al.*, 1998] and allow for intuitive analysis of observed gravity wave events and interpretation of numerical model results.

3. Numerical Model

[35] One of the most notable features of vertically propagating gravity waves is the exponential increase in wave magnitude due to the exponential decrease of background atmospheric density with altitude. This wave growth can lead to significant nonlinear effects, convective or dynamic instability, and wave breaking. It is therefore necessary to use a numerical scheme which remains stable for steep or large-magnitude perturbations and is able to cope with spectral cascades to smaller scales associated with wave breaking processes [e.g., *Andreassen et al.*, 1994; *Franke and Robinson*, 1999]. This is particularly important in the middle atmosphere where the effects of physical diffusion are weak at the wave scales of interest. Given these concerns, we adopt a numerical scheme that can solve the fully nonlinear Euler equations for an invisicid atmosphere, while maintaining numerical stability with minimal application of artificial diffusion. This solution is then supplemented with external solutions for physical atmospheric diffusion processes.

3.1. Equations of Motion

[36] The Euler equations describe the nonlinear motion of an inviscid ideal gas. Physically, they express the conservation of mass density, momentum, and energy. These can be written in generalized form, including the effects of gravity, and neglecting the effects of rotation [e.g., *Hines*, 1960]:

$$\frac{\partial \rho}{\partial t} + \nabla \cdot (\rho \vec{v}) = 0 \tag{11}$$

$$\frac{\partial}{\partial t}(\rho \vec{v}) + \nabla \cdot (\rho \vec{v}\vec{v}) = -\nabla p - \rho \vec{g} \tag{12}$$

$$\frac{\partial E}{\partial t} + \nabla \cdot \{(E + p)\vec{v}\} = -\rho g v_z \tag{13}$$

[37] An approximation accounting for effects of viscosity in equation (12) will be discussed later. The energy equation and the equation of state for an ideal gas are defined as [*LeVeque*, 2002, p. 293–295]:

$$E = \rho\epsilon + \frac{1}{2}\rho(\vec{v} \cdot \vec{v}) \tag{14}$$

$$\epsilon = \frac{p}{(\gamma - 1)\rho} \tag{15}$$

where ρ is density (kg/m^3), p is pressure (N/m^2), $\vec{v}$ is the fluid velocity (m/s). The energy density E and specific energy density ε are expressed in (J/m^3) and (J/kg $\cdot$ m^3), respectively. Additional equation describing approximate viscous and eddy diffusion and thermal conduction processes can be written in the form:

$$\frac{\partial \vec{v}}{\partial t} = \nu \nabla^2 \vec{v} \tag{16}$$

$$\frac{\partial T}{\partial t} = \kappa \nabla^2 T \tag{17}$$

where T denotes temperature in Kelvin (derived from the ideal gas law), ν is the kinematic viscosity, and κ is thermal conductivity. These equations are solved separately from the Euler equations of inviscid gas dynamics and their implementation is described in section 3.4.

[38] For our numerical model to be statically stable at thermospheric altitudes, it is necessary to compensate for changes in atmospheric chemical composition with altitude. The ratio of specific heats γ (equal to 7/5 for a diatomic gas and 5/3 for a monatomic gas) is specified to vary with altitude to compensate for the transition from molecular to atomic oxygen occurring in the lower thermosphere. Variations of the mean molecular mass are also considered when defining the initial atmospheric state. Using the MSISE90

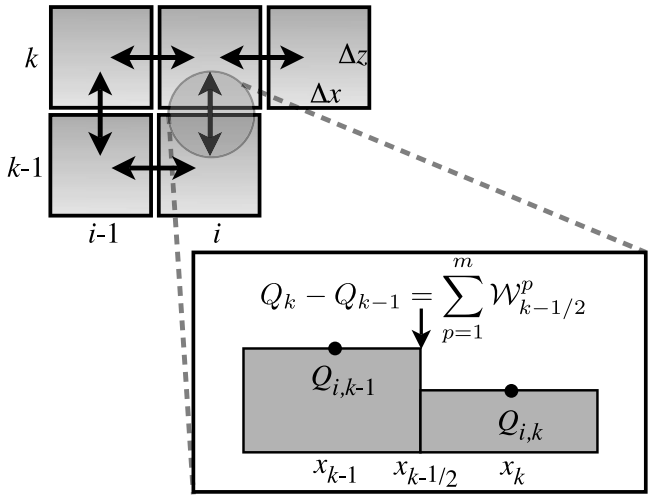

Figure 2. Schematic of 1-D Riemann problem solved between interface of two finite volume cells; eigenvalue and eigenvector decomposition yields solution for fluxes arising from the discontinuity between cells [*LeVeque*, 2002, p. 93].

[*Hedin*, 1991] profile, [O], [O_2], and [N_2] are assumed to be major species densities, and the approximate total major species density is given by [M] = [O]+[O_2]+[N_2]. Therefore we estimate γ using a simple weighted average:

$$\gamma = \frac{1.4([\mathrm{M}] - [\mathrm{O}]) + 1.67[\mathrm{O}]}{[\mathrm{M}]} \tag{18}$$

along with mean molecular mass:

$$\bar{M} = \frac{28[\mathrm{N_2}] + 32[\mathrm{O_2}] + 16[\mathrm{O}]}{[\mathrm{M}]} \tag{19}$$

[39] Using temperature T and mass density ρ given by MSISE90, we create a stable atmospheric profile by assuming the ideal gas law to define pressure $p = \rho RT/\bar{M}$, where $R \simeq 8.31\ \mathrm{J}\cdot K^{-1}mol^{-1}$ is the universal gas constant; from this expression for pressure, along with the model ρ and estimated γ, we solve for internal energy density E.

3.2. Numerical Method

[40] As a system of conservation laws, equations (11) through (15), describing conservation of density, momentum, energy, and state, may be expressed in a compact conservation law form in two dimensions [*LeVeque*, 2002, p. 431]:

$$\frac{\partial Q}{\partial t} - \frac{\partial F}{\partial x} - \frac{\partial G}{\partial z} = \psi \tag{20}$$

where

$$Q = \begin{bmatrix} \rho \\ \rho v_x \\ \rho v_z \\ E \end{bmatrix}; F = \begin{bmatrix} \rho v_x \\ \rho v_x^2 + p \\ \rho v_x v_z \\ v_x(E+p) \end{bmatrix}; G = \begin{bmatrix} \rho v_z \\ \rho v_x v_z \\ \rho v_z^2 + p \\ v_z(E+p) \end{bmatrix}$$

[41] Without the source term Ψ these equations describe the inviscid, nonlinear motion of an ideal gas. The source term Ψ in equation (20) introduces the effects of gravity, thereby facilitating buoyant wave motion, and can be expressed in the form:

$$\Psi = \begin{bmatrix} 0 \\ 0 \\ -\rho g \\ -\rho v_z g \end{bmatrix} \tag{21}$$

[42] This source vector neglects the viscosity term, which must be solved separately. The equation (20) is a system of conservation laws which may be reexpressed in terms of Jacobian matrices $A = \frac{\partial F}{\partial Q}$ and $B = \frac{\partial G}{\partial Q}$:

$$\frac{\partial Q}{\partial t} - A\frac{\partial Q}{\partial x} - B\frac{\partial Q}{\partial z} = \Psi \tag{22}$$

[43] If $\Psi = 0$ and both A and B are diagonalizable with real eigenvalues then the system is said to be hyperbolic [*LeVeque*, 2002, p. 31]. The Euler equations above may be solved with any one of many numerical schemes suitable for hyperbolic problems. Hyperbolicity is not maintained when the system includes diffusion (e.g., the Navier Stokes equations), hence this term has been separated to allow use of the finite volume numerical scheme.

[44] The model is implemented in the CLAWPACK software package (http://www.amath.washington.edu/∼claw) [*LeVeque*, 2002, pp. 87–99], which includes the generalized portions of the method such as the time-stepping system, the cell updating algorithms, and the flux limiters. Versions of CLAWPACK exist for one-, two-, and three-dimensional systems and support features such as adaptive mesh refinement and parallel processing through MPI (message passing interface). Fluxes in LeVeque's method are determined by solving an initial value problem, called a Riemann problem, to obtain fluxes resulting from the discontinuity between any two neighboring cells. This is shown schematically in Figure 2. The Riemann problem is expressed as a characteristic decomposition of the difference between neighboring cell averages:

$$Q_k - Q_{k-1} = \sum_{p=1}^{m} \alpha^p_{k-1/2} r^p_{k-1/2} = \sum_{p=1}^{m} \mathcal{W}^p_{k-1/2} \tag{23}$$

where the characteristic wave fluxes $\mathcal{W}^p_{k-1/2}$ are expressed as $r^p_{k-1/2}$, the pth eigenvector of A or B, as defined previously, multiplied by a magnitude coefficient $\alpha^p_{k-1/2}$. The eigenvalues of matrix A and B, $s^p_{k-1/2}$, denote the speeds of the characteristic waves. These quantities are then used by CLAWPACK to determine flux updates between neighboring grid cells.

[45] Since steady-state stability is crucial in a model spanning many atmospheric regions, we account for the gravity terms using LeVeque's flux-differencing "f-wave" propagation method [*Bale et al.*, 2002; *LeVeque*, 2002, pp. 333–337, 399–401]. Here, the Riemann problem in the stratified atmosphere is solved differently for horizontally and vertically adjacent cells. In the horizontal direction, the neighboring cells' equilibrium values are identical, and they are automatically in balance. In the vertical direction, cells are balanced by buoyant and gravitational forces.

The Riemann problem is then expressed as a characteristic decomposition of flux differences between each cell:

$$G_k(Q_k)G_{k1}(Q_{k1}) - \Delta z\Psi_{k-1/2} = \sum_{p=1}^{m} s^p_{k-1/2}\alpha^p_{k-1/2}r^p_{k-1/2} \quad (24)$$

[46] The variable $s^p_{k-1/2}$ is the speed (eigenvalue of matrix A or B) of the characteristic wave $\mathcal{W}^p_{k-1/2}$, which is the pth eigenvector of A or B multiplied by a magnitude coefficient $\alpha^p_{k-1/2}$. The eigenvalues $s^p_{k-1/2}$ may be calculated explicitly as a means to extract ${\mathcal{W}_{k-1/2}}^p$ from $\mathcal{Z}^p_{k-1/2} = s^p_{k-1/2}\alpha^p_{k-1/2}r^p_{k-1/2}$. The Riemann problem cannot be solved linearly for the Euler equations, so the Roe averaged solver is used [*Roe*, 1981; *LeVeque*, 2002, pp. 317–323]. This yields the characteristic waves and speeds, which are then used by LeVeque's CLAWPACK software package to calculate fluxes of physically conserved quantities between neighboring cells. The Roe solver used in the numerical model is based on that provided in CLAWPACK, although modified to use the "f-wave" method for inclusion of gravity source terms. Details of this balancing method were originally presented by *Bale et al.* [2002] and *LeVeque* [2002, pp. 399–401].

3.3. Boundary Conditions

[47] It has been common in previous numerical studies to examine gravity waves in spatially periodic domains. The Earth effectively provides a periodic domain for long-range or large-scale gravity wave propagation. In global studies [e.g., *Mayr et al.*, 1984], it is necessary to model large-scale gravity wave propagation under natural periodic conditions. For waves which are studied here, global propagation is made nearly impossible by dissipation and large-scale wind dynamics, thereby obviating the need for a large domain. For previous detailed studies of small-scale gravity waves, periodic computational domains spanning single horizontal wavelengths have been employed to allow higher resolutions [e.g., *Franke and Robinson*, 1999]. Some additional numerical concerns arise in a small spatially periodic domain. In a periodic domain, a packet which is modifying the structure of the local atmosphere experiences a feedback effect as it propagates continuously over a finite region, without natural horizontal dispersion. While this description becomes accurate for very long wave trains, it will otherwise exaggerate nonlinear accelerations of the mean flow that may be of less significance for packets that are horizontally finite, spanning just a few wavelengths. Furthermore, the use of a periodic domain may impose constraints on horizontal wave numbers, favoring those which satisfy spatial harmonics of the model domain. For these reasons, we employ "open" simulation domain boundaries.

[48] Boundary conditions are based on simple outflow conditions for the Euler equations [*LeVeque*, 2002, pp. 129–131]. Without stratification, this involves extrapolation of outer cell values at the boundaries, such that fluxes are zero into the domain. With stratification, we assume that quantities may be scaled in accordance with the vertical increase in perturbation magnitude associated with the decrease in background density and pressure. A scaling factor is introduced to extrapolate the dynamic perturbations to each conservative quantity (ρ, $\rho\vec{v}$, or E) at the upper and lower boundaries, which is then added to the steady state value stored in a reference array. For waves propagating with phase fronts parallel to the side boundaries, this extrapolation remains valid and effectively serves as an outflow condition. For most gravity waves, which propagate with a component perpendicular to these boundaries, the anisotropy between vertically adjacent cells will result in slight reflection from lateral boundaries.

[49] It is conventional to use Rayleigh friction sponge layers to damp waves as they approach boundaries, hence reducing the magnitudes of any reflected waves. Initial results presented using a similar numerical model [*Snively and Pasko*, 2003, 2005] have employed sponge layers along the vertical and lateral boundaries of the simulation domain. However, for most results presented in this paper (excluding the wave tunneling solution used for model validation in case study I), we include models of molecular viscosity and thermal conduction. This significantly damps waves in the thermosphere, thereby reducing artificial reflection and influence of reflected wave energy. Diffusion, along with careful source placement away from lateral boundaries, allows us to avoid the use of sponge layers for case studies IIa and III, where the spectrum is sufficiently focused to confine breaking to a predictable region in space. For case studies I and IIb, the sponge layers are identical to those used by *Snively and Pasko* [2003].

3.4. Dissipative Effects

[50] Ignoring eddy-diffusion, the dominant diffusion processes above 100 km arise simply from molecular viscosity and thermal conductivity of the rarefied atmosphere. The related coefficients are modeled as being inversely proportional to the atmospheric density [*Gossard and Hooke*, 1975, p. 220]. While the dynamic viscosity η does not change significantly with altitude, kinematic viscosity $\nu = \eta/\rho$ is inversely proportional to density and therefore increases exponentially with altitude. At lower altitudes (below ~110 km), the kinematic viscosity is fixed at a value which is comparable to, or slightly greater than, measured eddy diffusion throughout the middle atmosphere (100 m^2s^{-1}) [e.g., *Hocking*, 1990, *Fukao et al.*, 1994]. The thermal diffusivity term κ is related to the molecular kinematic viscosity ν by a factor of 1.5, assuming prevalence of molecular oxygen (monatomic gas) at altitudes above mesopause where diffusion will be most relevant [*Hines*, 1974, p. 382]. Figure 3 depicts model diffusivity profiles. We use simplified expressions for viscous and thermal diffusion effects, given by equations (16) and (17), respectively, which neglect compressibility and terms arising from spatial variations of coefficients. To maintain a stable background profile, diffusion is only applied to perturbations beyond the initial background state. Equations (16) and (17) are solved using an explicit first-order finite-difference method, following each time step of the CLAWPACK solution for equations (11)–(13). The model results are not sensitive to exact diffusion profiles; however, the presence of strong diffusion above 100 km does result in visible smoothing of small-scale wave solutions.

3.5. Gravity Wave Source

[51] The gravity wave source models the convective oscillations associated with a thunderstorm [*Fovell et al.*, 1992], using a standing wave oscillator [e.g., *Snively and Pasko*, 2003, 2005]. The source introduces a Gaussian

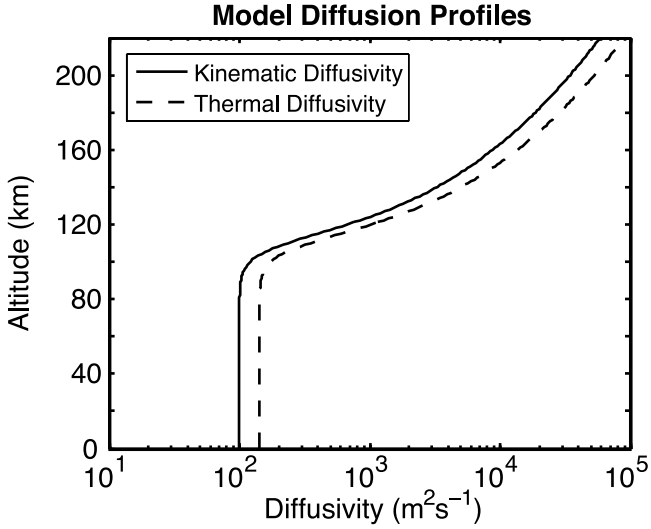

Figure 3. Model diffusivity profiles for kinematic viscosity, including approximate eddy diffusion and molecular diffusion effects.

frequency spectrum centered at the period $\tau = 2\pi/\omega$, with characteristic horizontal wavelength of $\lambda_x = 2\pi/k_x$. The wave forcing function $F_s(x,z,t)$ is introduced as a term on the right side of the vertical momentum equation.

[52] Half-widths of a Gaussian envelope in time (σ_t) and space (σ_x, σ_z) are defined, and a horizontal sinusoidal variation is introduced to enforce a wavelength $\lambda_x = 2\pi/k_x$ for a source magnitude of $\mathcal{F}_o$:

$$F_s(x,z,t) = \mathcal{F}_o \exp\left(-\frac{(x-x_0)^2}{2\sigma_x^2} - \frac{(z-z_0)^2}{2\sigma_z^2} - \frac{(t-t_o)^2}{2\sigma_t^2}\right) \cdot \cos(k_x x)\cos(\omega t) \quad (25)$$

[53] Variables x_o, z_o, and t_o represent the locations of the source maxima in space and time, respectively. The source spectrum is sufficiently narrow such that it will not excite the second harmonic of the forcing frequency. The source is effectively a standing-wave oscillator (radiating in both horizontal directions), as there is no horizontal phase progression over time. It has no explicitly prescribed vertical wavelength, and the vertical scale of radiated waves is expected to be closely determined by the gravity wave dispersion relationship given background wind U, the Brunt-Väisälä frequency N of the upper troposphere along with the horizontal wave number k_x and frequency ω specified for the oscillatory source. Horizontal wave number may also be specified as 0, as done in case study IIb. The source then becomes a spatially Gaussian oscillator, with wave number spectrum arising naturally from the forced frequency spectrum and local atmospheric structure.

4. Ambient Atmosphere and Model Parameters

[54] In this paper three sets of simulation results are reported, each illustrating the excitation of a lower-thermospheric ducted wave by a tropospheric source. Results describe linear duct coupling, nonlinear excitation against the direction of wind flow by breaking primary waves of narrow and broad spectra, and nonlinear excitation along the direction of wind flow by breaking primary waves, as outlined at the end of section 1. These model runs are henceforth termed case study I, IIa,b, and III, respectively. The related ambient atmospheric conditions and model run parameters are presented below.

[55] For each case study, wind velocity is assumed to be constant throughout the model domain. This permits simple analysis of modes and dispersion properties, allowing us to choose parameters based on analytical solutions. Although this assumption is never valid in the Earth's atmosphere, it appears to be a reasonable approximation for localized background conditions that often support meridionally propagating thermally ducted waves. Similarly, the wind flow observed during the event reported by *Taylor et al.* [1995], which motivates case study II, was relatively weak in the direction of wave propagation, allowing thermal-ducting effects to dominate [e.g., *Munasinghe et al.*, 1998]. Alternatively, wind flow may often block vertical gravity wave propagation, causing premature reflection or critical level dissipation. Varying winds throughout the middle and upper atmosphere are also able to support Doppler ducts [e.g., *Chimonas and Hines*, 1986; *Fritts and Yuan*, 1989; *Isler et al.*, 1997], which are not considered here. A case study where wind flow is found to strongly determine ducted wave propagation and structure has been presented recently by *Snively et al.* [2007].

4.1. Case Study I (Validation): Linear Coupling Between Ducts

[56] The first case study, based on results of *Walterscheid et al.* [2001], is presented as validation of the linear behavior of the analytical and numerical models presented in sections 2 and 3, respectively. This model run involves the simulation of coupling between ducted wave modes. While much of the mesosphere presents a region of evanescence for waves of $\tau \sim 6$ min, it is possible that wave energy may transfer from the stratospheric duct to the lower-thermospheric duct by a linear tunneling through this region. For optimal transfers to occur, there should be an intersection in the duct characteristics near the excitation frequency, such that the ducts' modal dispersion curves overlap at some values of ω and k_x [*Jones*, 1970; *Fritts and Yuan*, 1989]. This process is shown schematically in Figure 4a and illustrated below in section 5.1 for both numerical and analytical models.

[57] The atmospheric profile is obtained from the MSIS-E-90 atmospheric model [*Hedin*, 1991] (http://nssdc.gsfc.nasa.gov/space/model/atmos/msise.html), which provides density (O_2, N_2, O, and total) and temperature data for a region and date of interest. The model profile is chosen to approximately match that used by *Walterscheid et al.* [2001] and is the same as used by *Snively and Pasko* [2003]. It is obtained for 15 June 2001, at noon local time, for a geographical latitude $-11°$ and longitude 131°. The model atmosphere has two distinct thermal ducts; a stratospheric duct at approximately 30 km and a lower thermospheric duct at an altitude of approximately 110 km.

[58] To obtain modal dispersion curves and approximate solutions for a realistic duct, as done in each case study presented in this paper, a simple procedure is followed. Given atmospheric conditions specified by the MSISE90

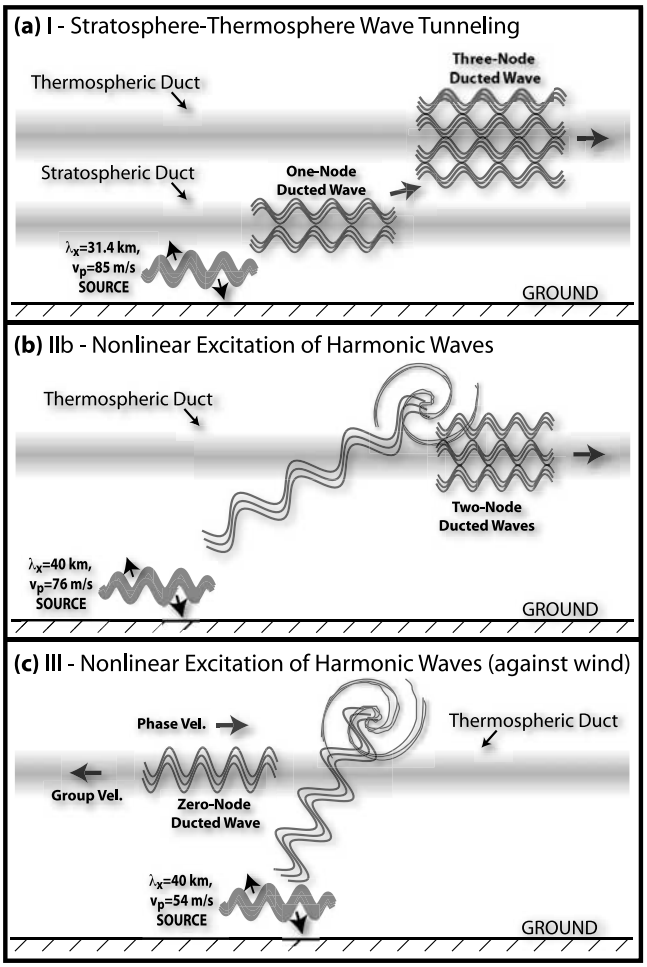

Figure 4. Schematic of model case studies I, II, and III illustrating: (a) linear coupling between stratospheric and lower-thermospheric ducts, (b) nonlinear excitation of ducted harmonic secondary waves by a breaking primary wave along the direction of wind flow, (c) nonlinear excitation of ducted harmonic secondary waves by a breaking primary wave against the direction of wind flow.

model [*Hedin*, 1991], the N^2 profile is obtained. For the atmospheric ducts of interest (e.g., lower thermospheric duct or stratospheric duct), the analytic N^2 profile given by equation (4) is fit to the profile obtained from the MSISE90 model. Figure 5a depicts the MSISE-90-derived Brunt-Väisälä frequency (dotted line) along with analytical profiles describing approximate Brunt-Väisälä frequency for both lower thermospheric and stratospheric ducts (solid lines). From these analytical N^2 profiles, modal dispersion curves are obtained using equations (8)–(10) along with analytic solutions [e.g., *Thorpe*, 1968].

[59] Figure 5b illustrates modal dispersion curves for the stratospheric and thermospheric ducted modes. In this case, a curve describing the dispersion properties of the stratospheric duct's $m = 2$ mode intersects with the thermospheric duct's $m = 4$ mode at a period of $\tau = 6.05$ min and horizontal wavelength of $\lambda_x = 31.4$ km. At this frequency and wavelength, assuming the ducts are in close proximity, the wave would be able to exchange ducts freely while satisfying a ducted mode solution in either duct. To confirm this process, we excite a wave packet with a Gaussian spectral peak satisfying the above parameters, using a standing-wave oscillatory source (equation (25)). The full set of numerical model parameters for case study I is listed in Tables 1 and 2. Forcing magnitude is chosen to be weak, such that the solution remains linear at all altitudes of the simulation domain. These simulated waves for this case study are weaker than those typically observed, but similar modes can exist at stronger magnitudes that are still below the threshold of instability.

4.2. Case Study II: Nonlinear Excitation, Downwind

[60] An alternative case exists for tropospherically generated waves with periods too long to be ducted; however, second harmonics of these waves may satisfy ducted mode solutions. This scenario has been described analytically for waves which propagate through varying atmosphere structure [*Chimonas et al.*, 1996]. A similar case has been studied numerically, where the primary wave breaks at an altitude just above mesopause [*Snively and Pasko*, 2003], as shown schematically in Figure 4b. In either case, the second harmonic is excited as a nonlinear product of the primary wave [e.g., *Chimonas et al.*, 1996; *Franke and Robinson*, 1999]. Here we consider a duct with a constant wind flow in the same direction as both primary and secondary wave propagation. We first examine the case where the primary wave is excited with specified frequency and wave number spectra (case study IIa), followed by the case where the primary wave is excited with a specified frequency spectrum but broadened wave number spectrum (case study IIb). For each case, breaking of the primary wave packet will occur at some altitudes above the duct, thereby maximizing the strength of nonlinear interaction without destroying the local duct structure. Total excited wave energies for case studies IIa and IIb are approximately equal.

[61] The ambient atmosphere for these model cases is obtained for the date and time of the ALOHA93 event reported by *Taylor et al.* [1995], 10 October 1993, at 1030 LT, for a geographical latitude 20.8° and longitude 203.8° using data from the MSISE-90 model [*Hedin*, 1991]. Wind velocity is assumed to be constant at 10.5 m/s. This value is identical to that used by *Snively and Pasko* [2005], and is consistent with the observed 10–17 m/s wind along the direction of wave propagation as measured by J. R. Isler (cited as private communication in the work of *Taylor et al.* [1995]). Justification for the choice of value for this parameter is described below.

[62] Plotted in Figure 6a is the MSIS-E-90-derived Brunt-Väisälä frequency (dotted line) along with analytical profiles describing approximate Brunt-Väisälä frequency for each duct (solid line). The model profile is identical to that used by *Snively and Pasko* [2005] in the study of ducted wave-induced airglow modulation. In each case, IIa and IIb, the ground-relative period and horizontal wavelength of the primary waves are $\tau = 8.8$ minutes. For case study IIa, the horizontal wave number is prescribed by a Gaussian centered at $\lambda_x = 40$ km, equal to twice the period and wavelength reported by *Taylor et al.* [1995]. For case study IIb, this horizontal wave number is not prescribed, but the

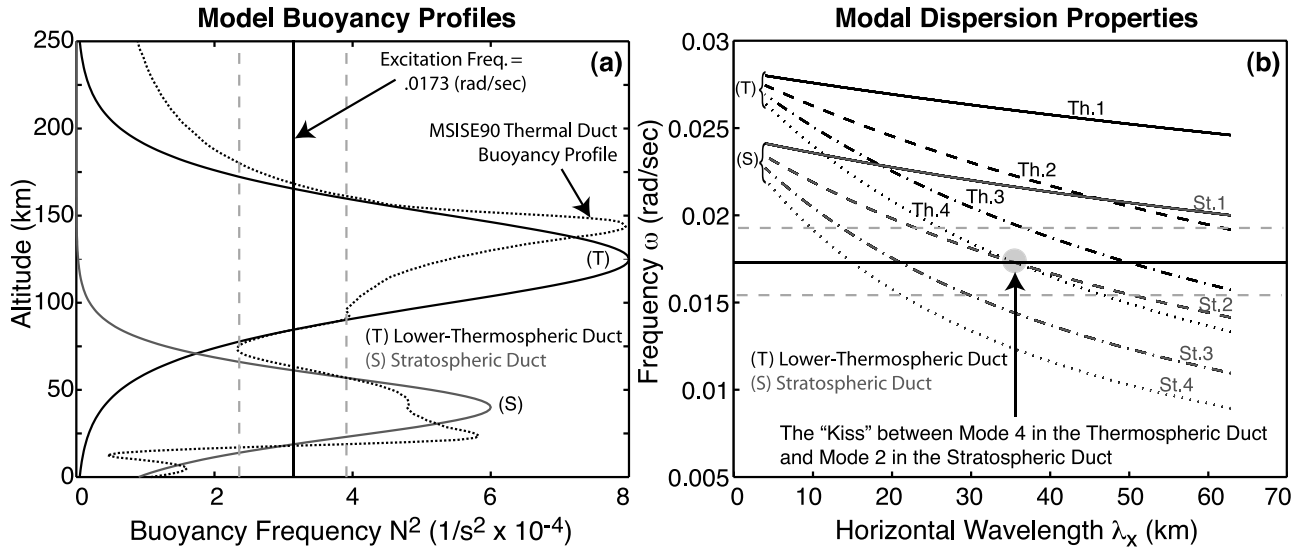

Figure 5. Analytical duct properties corresponding to case study I: (a) Altitude profile of the squared Brunt-Väisälä frequency for MSISE90 model and the analytical model ducts; (b) Dispersion properties of lower thermospheric and stratospheric ducts plotted for modes m = 1, 2, 3, and 4.

Gaussian source is specified to force a packet of equal energy to case study IIa, with similar frequency spectrum. The source is, effectively, a small Gaussian oscillator, yielding a broadened wave number spectrum. This example is provided for the sake of comparison. Parameters used by the numerical model for case studies IIa and IIb are outlined in Tables 1 and 2.

[63] As stated above, wind flow is specified as 10.5 m/s along the direction of wave propagation. This parameter was determined analytically using the duct model described in section 2.2. The modal dispersion curves, relating phase velocity and horizontal wavelength, are plotted in Figure 6b. Ducted wave modes with a horizontal wavelength of λ_x = 20 km and a horizontal phase velocity of 76–77 m/s were sought, consistent with the observation reported by *Taylor et al.* [1995]. The mode most closely satisfying these parameters is the m = 3, 2-node, waveguide mode. This is notably similar to the wave mode proposed first by *Munasinghe et al.* [1998] for explanation of observations reported by *Taylor et al.* [1995]. Since wind velocities were known approximately to be in the range ~10–17 m/s along the direction of wave propagation, the wind velocity U was obtained analytically to fit the dispersion curves to the observed wave properties given the duct spatial distribution. The result is the specified constant wind velocity of U = 10.5 m/s along the direction of short-period wave propagation. The results here are not sensitive to the exact wind velocity, as forcing occurs over a broad spectrum, allowing a range of wave phase velocities to be excited. Only a limited portion of the forced spectrum will identically satisfy ducted modes; however, a significant portion of the spectrum will propagate as nonideally ducted waves. Over long periods of time, the fully ducted modes will appear dominant due to dispersive filtering. Similar ducted wave modes arise for a broad range of possible wind profiles and magnitudes. A consistent spatially varying wind profile would be notably more physical (particularly if based on actual measurements or large-scale model data). However, it would preclude convenient use of an analytical model solution and comparison with previous model and experimental results [e.g., *Munasinghe et al.*, 1998].

4.3. Case Study III: Nonlinear Excitation, Upwind

[64] The ambient atmosphere for this model case is identical to that used for case studies IIa and IIb, however with a wind flow of 25 m/s rather than 10.5 m/s. Rather than studying waves excited in the direction of wind flow, we focus on those propagating against the wind flow, to the "left" of the source. These waves propagate against a wind flow of 25 m/s and are therefore Doppler shifted to higher intrinsic frequencies. The ground-relative phase and group velocities of the modal dispersion curves are accordingly reduced by 25 m/s.

[65] Figure 6a depicts the numerical and analytical models of Brunt-Väisälä frequency, with the analytical duct fit to the region of interest. These plots are based on the same model thermal profile as used for case study II, however with a different analytical profile. Therefore, the model profile is identical except for increased wind flow, while the analytical profile assumes that ducting occurs in a slightly different region of the atmosphere due to the higher frequencies of interest. Figure 6b illustrates group and phase velocity modal dispersion curves arising from the specified analytical duct profile. Note that the wind is specified as −25 m/s, as we consider waves traveling against the direction of flow. The Doppler-shifted thermospherically ducted wave mode which we will consider, with 0 nodes

Table 1. Domain Parameters Used in Numerical Model

	x_{size} (cells)	z_{size} (cells)	Δx (km)	Δz (km)
Case study I	400	220	3	1
Case study II a,b	1600	220	1	1
Case study III	1600	220	1	1

Table 2. Source Parameters Used in Numerical Model

	τ (min)	λ_x (km)	σ_x (km)	σ_z (km)	σ_t (s)	x_o (km)	z_o (km)	t_o (s)	$\mathcal{F}_o/\rho$ (m^4s^{-2})
Case study I	6.05	31.4	30	3	2000	600	12	600	$\rho^{-1} \times 10^{-7}$
Case study IIa	8.8	40	30	4	2000	600	12	600	2.5×10^{-4}
Case study IIb	8.8	∞	1.5	4	2000	600	12	600	2.5×10^{-3}
Case study III	12.3	40	30	4	2000	600	12	600	1.75×10^{-4}

and λ_x = 20 km horizontal wavelength, exhibits a ground-relative phase velocity of 54 m/s. However, the ground relative group velocity of this wave is shifted to −20 m/s by the strong opposing wind flow. Therefore, when this wave mode is excited, the group and phase velocities will have opposite sign in the ground-relative frame. As noted in section 2.2, this is a simple example of a wave packet where energy and phase propagate in opposing horizontal directions, loosely analogous to electromagnetic propagation in media of negative refractive index [e.g., *Veselago*, 1968; *Cummer*, 2003].

[66] Initial parameters are chosen to excite a primary wave packet which is able to excite the desired secondary wave. With ground-relative phase velocity of 54 m/s and horizontal wavelength of λ_x = 40 km, the primary wave is excited by the standing wave oscillator with period of 12.34 min. While we have chosen an exact value for the sake of comparison, similar waves will be excited for a broad range of possible source spectra. Complete details of the parameters are outlined for this model case in Tables 1 and 2, and the model configuration is shown schematically in Figure 4c (Figure 7).

5. Results and Discussion

5.1. Case Study I (Validation): Linear Coupling Between Ducts

[67] Figure 8a depicts the wave as it is excited in the troposphere. The source oscillator, active from approximately 800 to 3200 s of the simulation run, excites a propagating gravity wave packet, which becomes trapped between the tropopause and the stratopause. The packet spectral peak corresponds closely to the m = 2 waveguide mode (two antinodes, one node) of the stratospheric duct. This ducted wave then leaks energy upward toward the lower thermospheric duct, tunneling through the evanescent boundary region near mesopause (Figure 8b). This forms a ducted gravity wave mode in the lower-thermospheric duct. In this case, as predicted, it is the m = 4 mode which is visibly dominant (four antinodes, three nodes). As the ducted waves propagate horizontally, as shown in Figure 8c, the coupling between modes persists, with energy transferring periodically upward and downward between ducts. The normalized perturbation magnitudes shown in Figures 8 correspond to very weak actual velocity and temperature perturbations in the atmosphere, therefore enforcing linearity of the obtained solution throughout the model domain.

[68] Having calculated in section 4.1 the frequency and wavelength at which mode coupling occurs, in addition to the duct's modal dispersion curves, analytical solutions can be plotted to compare with the numerical model results. The numerical solution for the second waveguide mode of the stratospheric duct and the fourth waveguide mode of the lower thermospheric duct are shown in Figure 8c. Figure 9a shows the analytical solution plotted for an arbitrary time, which may be compared with numerical model results in Figure 9b. Taking a single vertical column of data from the simulation results, a one-dimensional

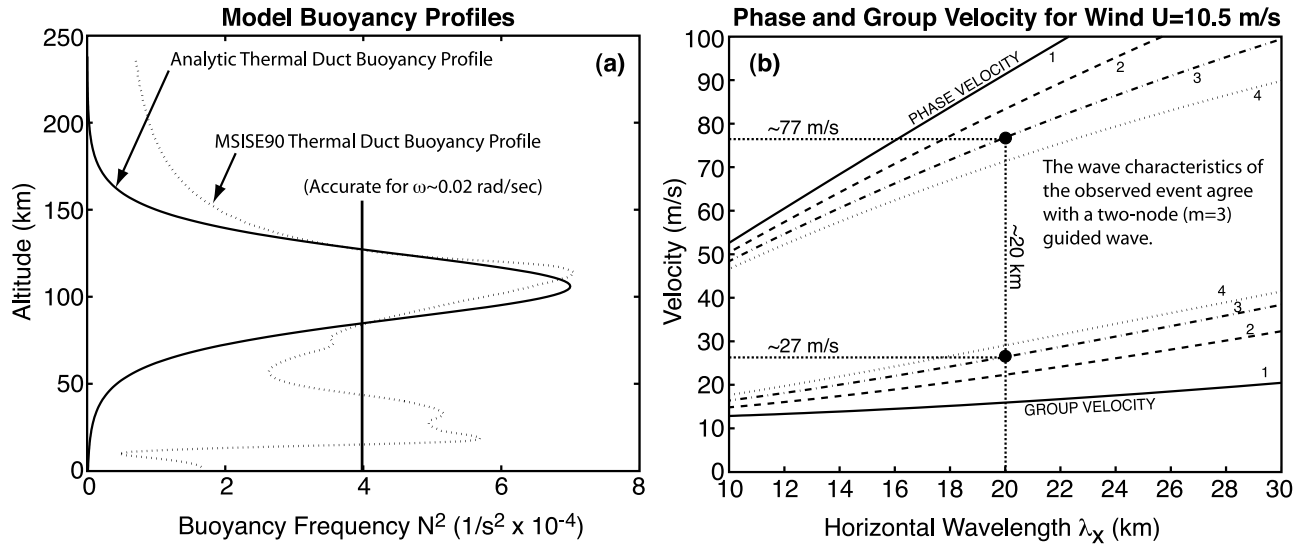

Figure 6. Analytical duct properties corresponding to case study II, which includes wind flow of 10.5 m/s: (a) Altitude profile of the squared Brunt-Väisälä frequency for MSISE90 model and the analytical model duct; (b) Dispersion properties of lower thermospheric duct plotted for modes m = 1, 2, 3, and 4, describing both group and phase velocities.

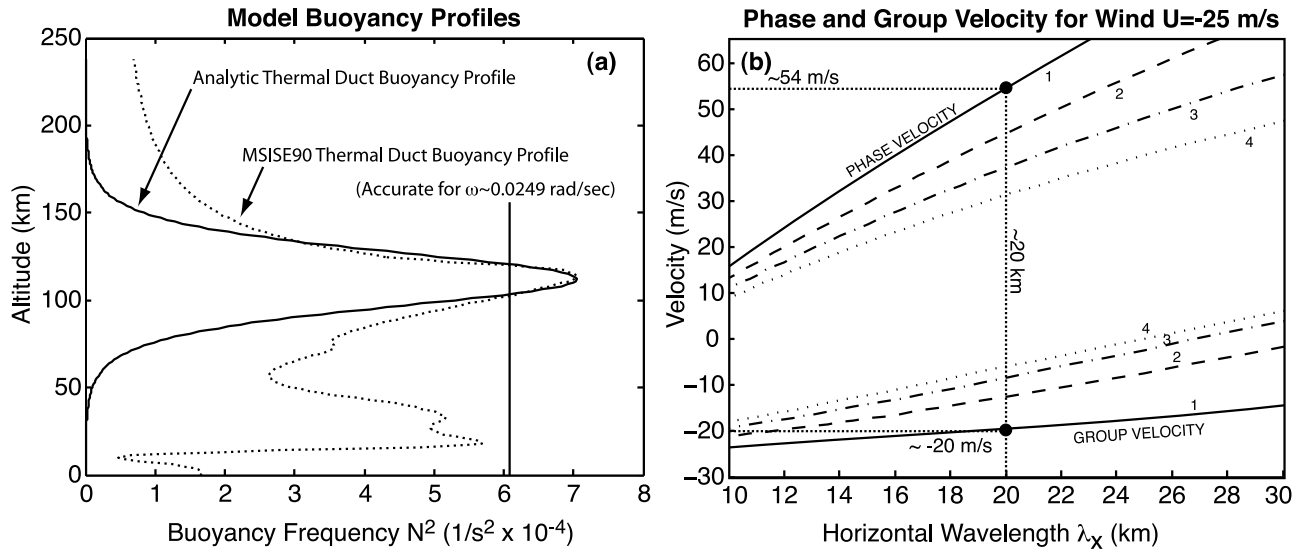

Figure 7. Analytical duct properties corresponding to case study III, which includes wind flow of −25 m/s: (a) Altitude profile of the squared Brunt-Väisälä frequency for MSISE90 model and the analytical model duct; (b) Dispersion properties of lower thermospheric duct plotted for modes m = 1, 2, 3, and 4, describing both group and phase velocities.

solution is plotted for normalized vertical velocity in Figure 10, illustrating consistency between the analytical and numerical solutions. These results are also consistent with previous results of *Fritts and Yuan* [1989] and *Walterscheid et al.* [2001], demonstrating coupling between stratospheric duct and lower thermospheric ducts. The similarities between analytical and two-dimensional numerical results presented here, and with *Walterscheid et al.* [2001], provide validation of the linear behavior of the employed analytical and numerical models presented in sections 2 and 3, respectively. Despite the low wave magnitude simulated here, ducted wave tunneling is likely to play a significant role in providing coupling between various thermal and Doppler ducts throughout the middle atmosphere.

5.2. Case Study II: Nonlinear Excitation, Downwind

[69] Figure 11a depicts the primary wave at t = 7500 s propagation time, following its generation by the oscillatory source of Case Study IIa, which peaked at t = 2000 s. The magnitude of the primary wave has led to the onset of breaking and overturning above the duct. Downward reflection of the primary wave below the breaking region is visible as a result of reduced local stability, which is further enhanced by the wave breaking at higher altitudes. The initial production of secondary waves, arising from the nonlinearity of the primary wave packet, leads to the small-scale wave structure visible in Figure 11b. By t = 10,500 s, the secondary wave is clearly visible propagating behind (and downward from) the primary wave in Figure 11c. The secondary wave packet has period and wavelength approximately half that of the primary wave and is trapped in the lower-thermospheric duct, as visible in Figure 11d. Over time, the various ideally and nonideally ducted secondary waves propagate and disperse through the duct, all propagating with slower group velocities (but nearly identical phase velocities) to the primary waves. The ducted secondary waves of higher-order modes propagate with faster group velocity, but slower horizontal phase velocity, than those of lower modes; this dispersion is visible in Figure 11e from 350−500 km horizontally. In Figure 11e, it is also clearly seen that components of both primary and secondary waves are ducted, however with the former trapped broadly between thermosphere and troposphere and the latter confined to a narrow region of the lower thermosphere.

[70] Figures 12a and 12b show vertical perturbation velocities taken at 110 km altitude over the durations of case study IIa and IIb, respectively. The measurement altitude is consistent with the approximate center of the lower thermospheric duct, with the time progression of the velocities presented along the vertical axis. Figure 12a illustrates the vertical velocity perturbation magnitudes of primary and resulting secondary waves modeled in case study IIa. Figure 12b illustrates the model evolution of vertical velocities for case study IIb, where the source wave number spectrum is slightly broadened. The secondary wave vertical velocities are comparable to, or slightly greater than, the primary wave magnitudes for case study IIa and IIb. Lines drawn at times t = 6600, 9000, and 11400 s correspond with line scans shown in Figures 13a, 13b, and 13c, respectively.

[71] Figures 13a, 13b, and 13c depict line scans of vertical fluid velocity for three times at 110 km for case studies IIa and IIb. Figures 13d, 13e, and 13f depict the associated wave number spectrum for three times at 110 km for case studies IIa and IIb. In Figure 13d, the primary wave is seen, with slightly higher horizontal wave number than predicted, and the wave number spectrum is broader in IIb than IIa (dashed line versus solid line, respectively). Figure 13e depicts the transition to higher wave number modes, with the expected $2k_x$ relationship of secondary waves to primary waves. The broadened spectrum of the primary wave in IIb leads to a broader spectrum of secondary waves. The signatures of both primary and secondary waves are

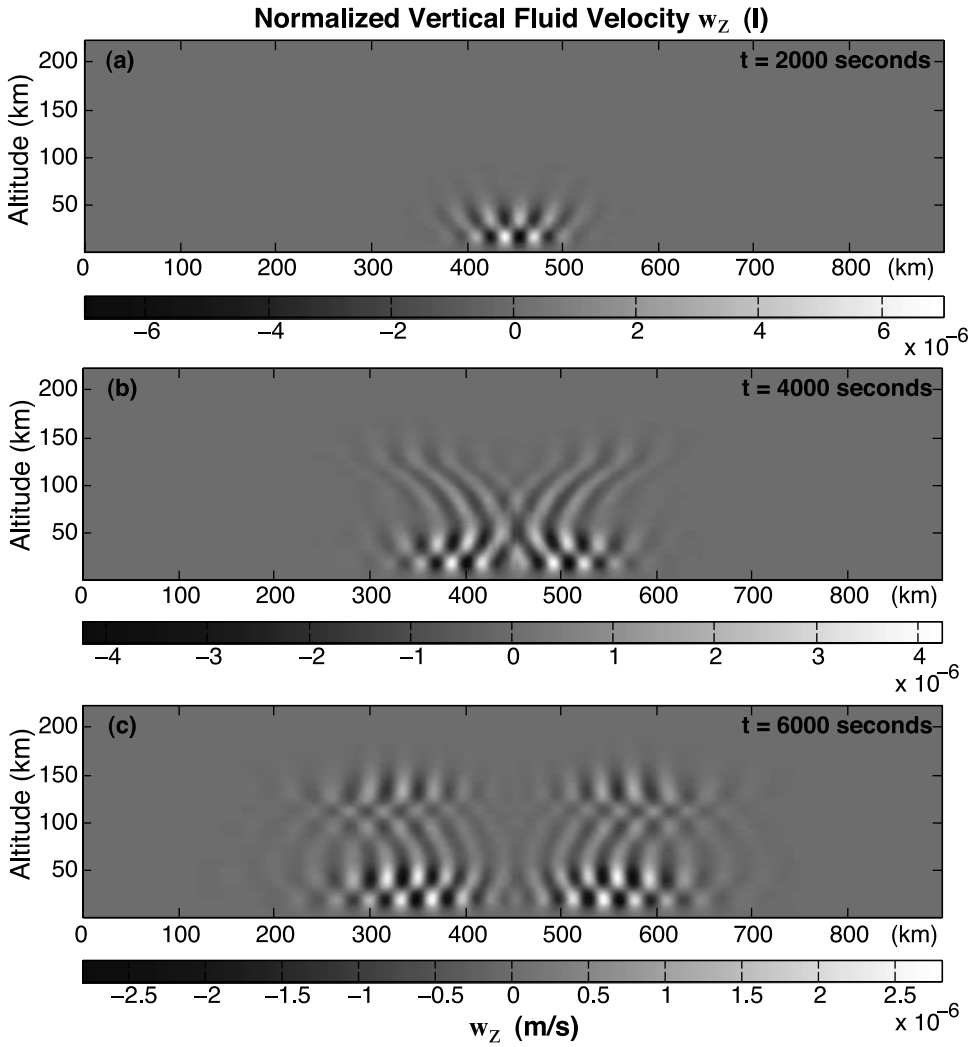

Figure 8. Vertical perturbation velocity field normalized by factor of $(\rho/\rho_o)^{1/2}$, plotted at three time instants of the case study I depicting (a) stratospheric ducted wave excitation, (b) vertical propagation into thermosphere, and (c) ducted wave propagation in both stratospheric and thermospheric ducts.

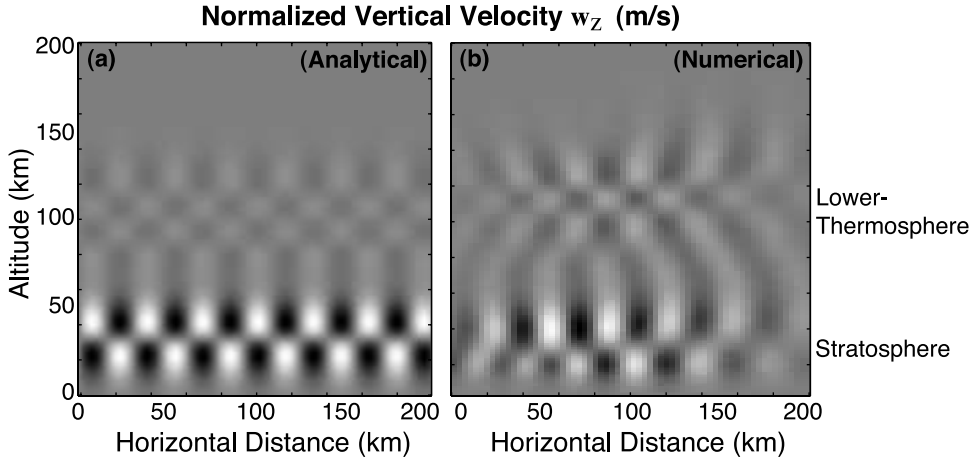

Figure 9. Normalized vertical perturbation velocity plotted for (a) analytical ducting models with $m = 2$ in stratosphere and $m = 4$ in thermosphere and (b) numerical model of tropospherically generated ducted wave propagating from stratosphere to lower thermosphere (case study I).

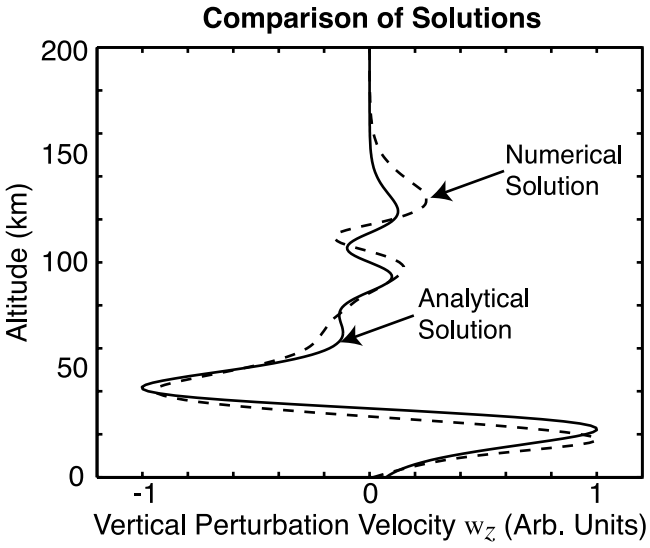

Figure 10. Normalized vertical perturbation velocity w_z: One-dimensional plot corresponding to vertical scan of Figure 9a and Figure 9b at $x \simeq 90$ km for analytical and numerical solutions, respectively.

visible in the evolving spectra, and the magnitude of the secondary waves is appreciable and would be easily observable. The primary wave magnitude decreases over time as it propagates out of the 110 km altitude region.

[72] To analyze the kinetic energy densities of the primary and secondary waves, we apply bandpass Hamming window filters to isolate their Gaussian horizontal wave number spectra of vertical and horizontal fluid velocities v_x and v_z. From these filtered quantities we obtain kinetic energy $\frac{1}{2}\rho(v_x^2+v_z^2)$, which is then horizontally averaged and normalized. Figure 14 depicts the normalized, horizontally averaged kinetic energy density, bandpassed separately for primary and secondary waves at 110 km, plotted over time for case study IIa. The local kinetic energy density at the primary wave number decreases as the packet propagates vertically beyond 110 km altitude. Subsequent oscillations in energy density occur due to partial downward and upward reflections of the primary wave, due to the periodicity of energy flux associated with nonideal reflection and ducting of the primary wave packet [e.g., *Yu and Hickey*, 2007]. Energy of the ducted secondary wave packet becomes apparent as it is excited, and as secondary wave energy from higher altitudes propagates downward to the measurement altitude (110 km). The energy density of the secondary wave packet is not insignificant, although it remains an order of magnitude lower than the peak energy density of the primary packet.

[73] The total kinetic energy transfer from the primary wave packet to the secondary wave packet is less than 10%, which is likely greater than what could occur under more realistic wind conditions. As noted above, the vertical velocity of the secondary waves is sufficient to be observable at airglow altitudes and may be higher depending on local atmospheric parameters. It is difficult to assess the energetic significance of the secondary wave excitation, due to the idealized nature of atmospheric parameters used here. But, as noted by *Chimonas et al.* [1996], the secondary waves do provide an observable signature, which will remains after the primary wave packet has departed the local region and/or dissipated.

[74] Figure 15a shows frequency spectral evolution for case study IIa in the center of the duct at 110 km. Figure 15b shows the significant presence of harmonic components of the primary wave, including some residual presence of the fundamental mode visible at earlier timesteps. The primary wave is not entirely destroyed by the interaction, and it propagates away from the secondary wave packet. At times after t = 15,500 s, the frequency spectrum at the point of measurement again shows a significant peak at the secondary wave frequency of ω = 0.024 rad/s.

[75] It is clear that the wave interactions leading to production of harmonic waves in case studies II are closely related to those predicted and modeled by, e.g., *Chimonas et al.* [1996] and *Franke and Robinson* [1999]. Simply, they arise from a nonlinear resonance triad interaction of the primary wave of horizontal wave number k_x and frequency ω, itself, and a secondary wave with $2k_x$ and 2ω. This process arises from nonlinear terms (i.e., $\vec{v}\vec{v}$) present in the Euler equations (11)–(13) [e.g., *Franke and Robinson*, 1999]. Efficiency of secondary wave excitation is maximized when the wave begins to break just above the duct. The overturning is indicative of reduced atmospheric stability, which causes partial downward reflection for the primary wave packet. This reflection helps to suppress continued breaking above and below that region, and facilitates further interaction, as opposed to instability. Nonlinear self-interactions of the primary wave therefore may occur for both upward propagating and downward reflected components. In the event that the primary wave were of sufficient magnitude to break fully inside the duct, the resulting reduction in local stability could limit ducted wave excitation. Under such conditions, body forcing may be expected to dominate over nonlinear wave interactions [e.g., *Vadas et al.*, 2003].

[76] A control case was also examined where wave breaking does not occur at any altitude in the simulation domain. In the nonbreaking case (not shown), secondary wave magnitudes are an order of magnitude weaker than the primary wave, where in case study II the secondary waves magnitudes are on the same order as the primary wave. We believe this disparity is due, in part, to three factors. First, the increased primary wave magnitude may be expected to increase the intensity of nonlinear interactions (proportional to the square of velocity), leading to more effective transfer of energy to the secondary waves [e.g., *Chimonas et al.*, 1996]. Second, the breaking primary wave forms a region of reduced stability above the duct. This leads to partial reflection of the primary wave, and further facilitates the nonlinear interactions. Third, the breaking primary wave may also radiate additional second-harmonic waves, independent of the presence of the duct [e.g., *Andreassen et al.*, 1994; *Franke and Robinson*, 1999].

[77] The simulation of breaking in two dimensions are limiting, in that transverse instabilities are suppressed [e.g., *Andreassen et al.*, 1994]. It is presently too computationally demanding to render detailed three-dimensional wave breaking over similar distances for discrete packets. Furthermore, it is not the goal of this paper to model the dynamic subtleties of wave packet breaking. It is the

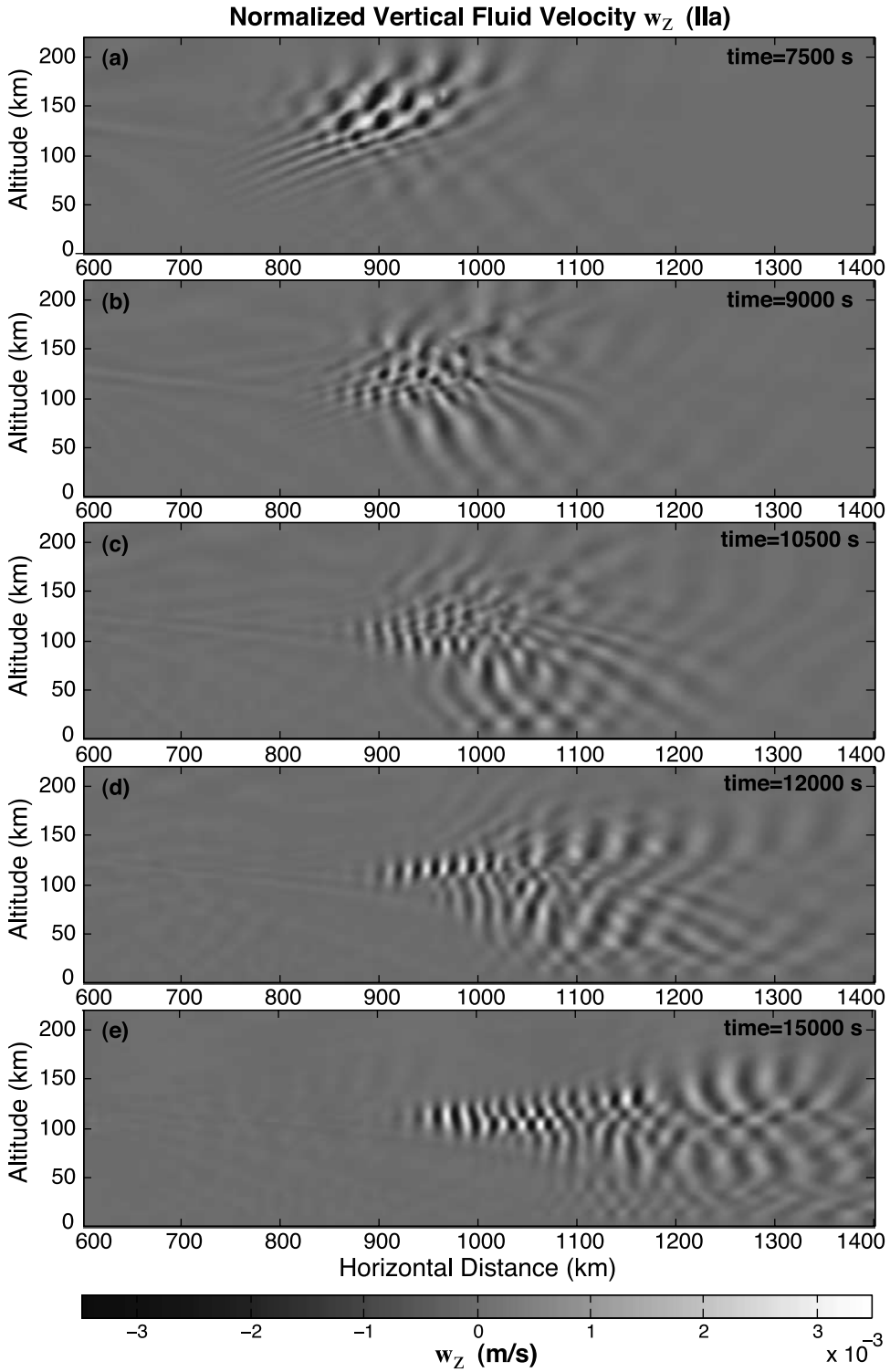

Figure 11. Normalized vertical perturbation velocity plotted for three time steps of case study IIa depicting (a) breaking of primary wave in lower thermosphere, (b) downward propagation of secondary wave from breaking region, (c, d) propagation of primary and secondary waves, (e) dispersive separation of secondary waves satisfying modes m = 1, 2, and 3.

formation of a region of reduced stability above the duct, which leads to partial downward reflection of the primary wave, and enhancement of nonlinear interactions inside the duct [e.g., *Chimonas et al.*, 1996; *Franke and Robinson*, 1999]. The simple convective instability processes leading to this effect do occur in two dimensions. Further three-dimensional instability modes would likely develop at larger magnitudes [e.g., *Fritts et al.*, 2006] and may destroy a greater portion of the wave packet at a faster rate [e.g., *Walterscheid and Schubert*, 1990; *Andreassen et al.*, 1994].

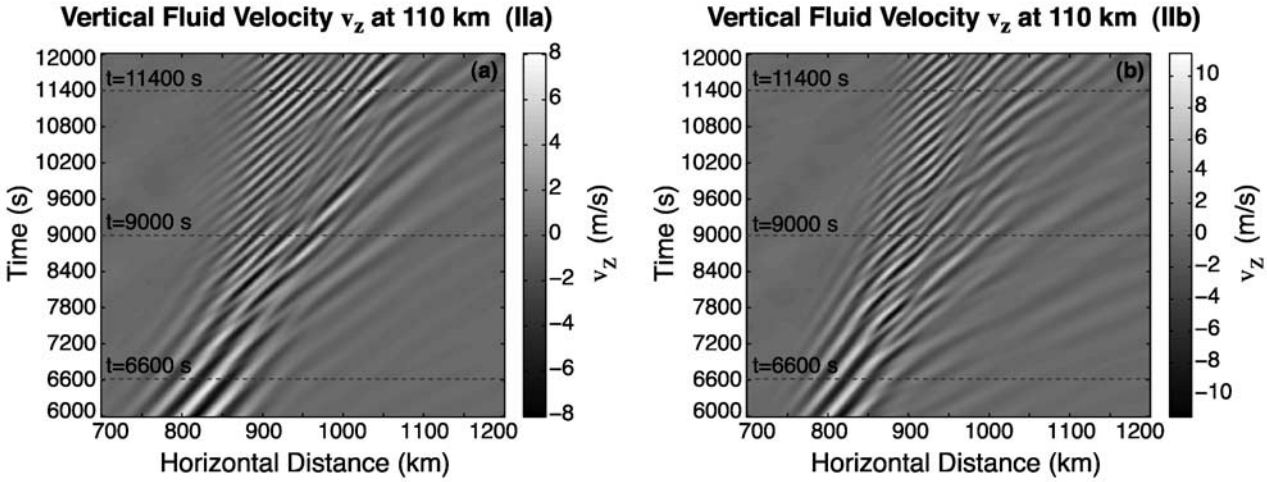

Figure 12. Time progression of vertical velocity taken at 110 km altitude and plotted over partial duration of simulation run for excitation of secondary waves by (a) fixed wave number spectrum (case study IIa) and (b) broad wave number spectrum (case study IIb).

The applicability and energetic significance of these processes in a three dimensional system should be investigated in the future.

5.3. Case Study III: Nonlinear Excitation, Upwind

[78] Figure 16a depicts the propagation of the primary wave into the wind, showing only the "left" portion of the simulation domain. The Doppler-shifted primary wave exhibits reflection in the lower thermosphere and above the troposphere, resulting in both upward and downward components of the wave. Here the primary wave has been shifted to higher intrinsic frequencies, resulting in longer vertical wavelengths. By the timestep illustrated in Figure 16b, minor wave breaking begins in the lower thermosphere due to large wave perturbation magnitude. In Figure 16c, the presence of the secondary wave packet is apparent behind the primary wave, however the secondary wave group propagates in the opposite ground-relative

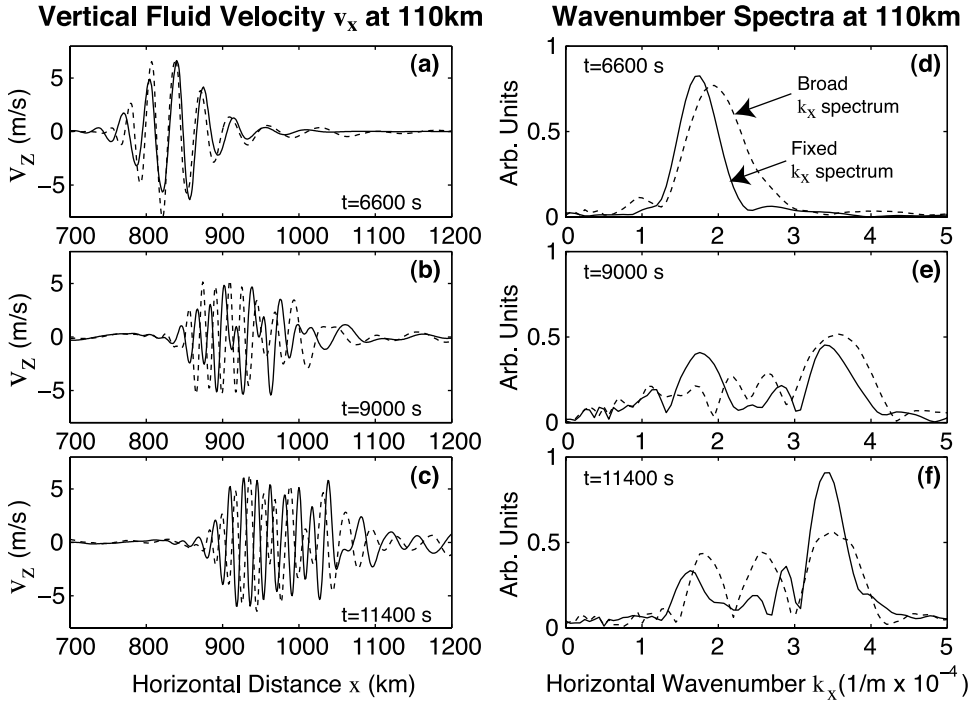

Figure 13. Vertical velocity line scans at 110 km (center of lower-thermospheric duct) for (a) $t = 6600$ s, (b) 9000 s, and (c) 11,400 s, respectively, taken before, during, and after excitation of secondary waves by a breaking primary wave for case study IIa (solid line) and IIb (dashed line). (d, e, f) Wave number spectra are illustrated, showing decrease of first harmonic intensity as the primary wave passes, and increase of second harmonic intensity as the secondary wave is excited.

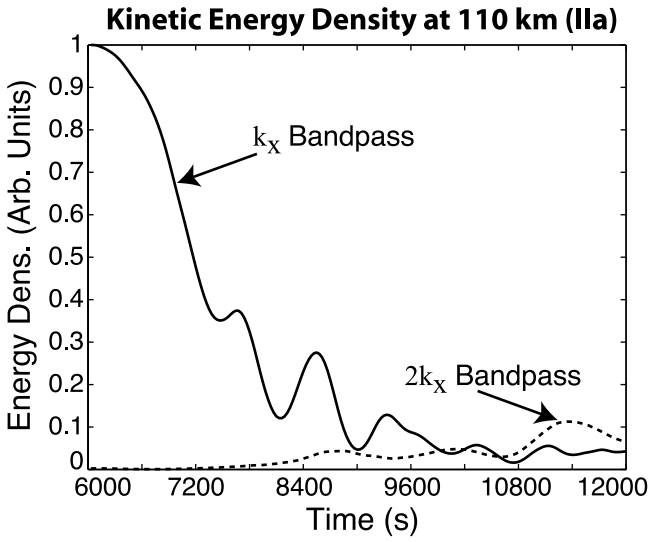

Figure 14. Horizontally averaged, normalized kinetic energy density at 110 km for the horizontal distance of 700 to 1200 km, illustrating the passage of primary wave energy (solid line) through the ducting region, and subsequent excitation of the secondary wave (dashed line).

direction as the primary wave. The ground-relative horizontal phase velocities of primary and ducted secondary waves are equal, at approximately 54 m/s.

[79] Figure 17a depicts the primary wave group and trailing secondary wave group. By this point in time, there is little interaction between wave packets. Figure 17b, taken at a later timestep, further demonstrates the opposite direction of group propagation. The secondary wave mode excited by the breaking/interacting primary wave is a 0-node mode (mode 1, single-antinode), however a weaker 1-node wave mode follows the ducted wave. The group velocity of the 1-node wave is also negative, although it is expected that its phase and group velocities are of lower magnitude than the 0-node wave packet.

[80] Figure 18 also illustrates the distinct negative ground-relative group velocity of the ducted packet, where the smaller-scale wave is clearly traveling in an opposite horizontal direction to the primary wave. Consequently, this ducted wave might be observed propagating alone, distinct from its primary source wave. Lines drawn at times t =

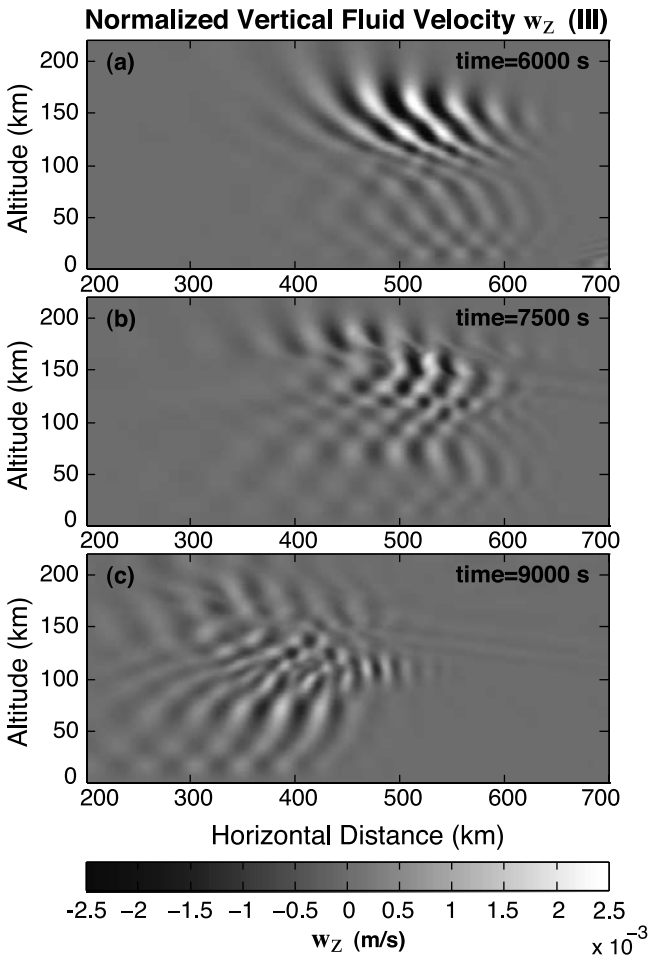

Figure 16. Normalized vertical perturbation velocity plotted for two instants of time for case study III depicting (a) primary wave propagation through middle atmosphere, (b) start of reflection and breaking at high altitude, and (c) breaking along with downward propagation of primary wave, with visible propagating secondary wave.

4500, 7500, and 10,500 s correspond with line scans shown in Figures 19a, 19b, and 19c, respectively.

[81] Figure 19 depicts line scans of vertical velocity at the times specified in Figure 18, along with the dynamic evolution of horizontal wave number spectra. Figure 19a

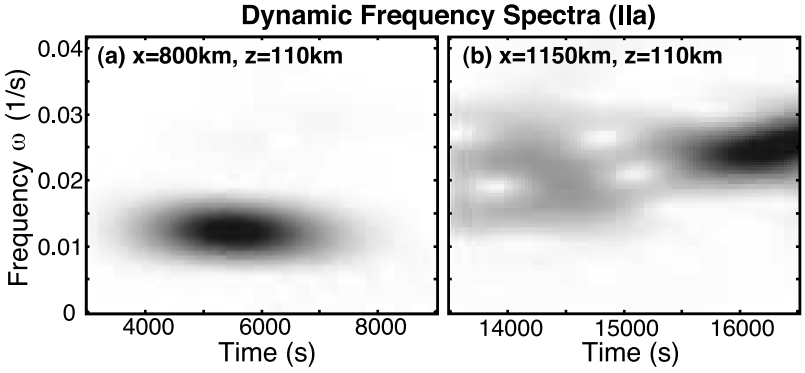

Figure 15. Dynamic frequency spectra taken (a) before and (b) after the excitation of secondary waves by a breaking primary wave for case study IIa.

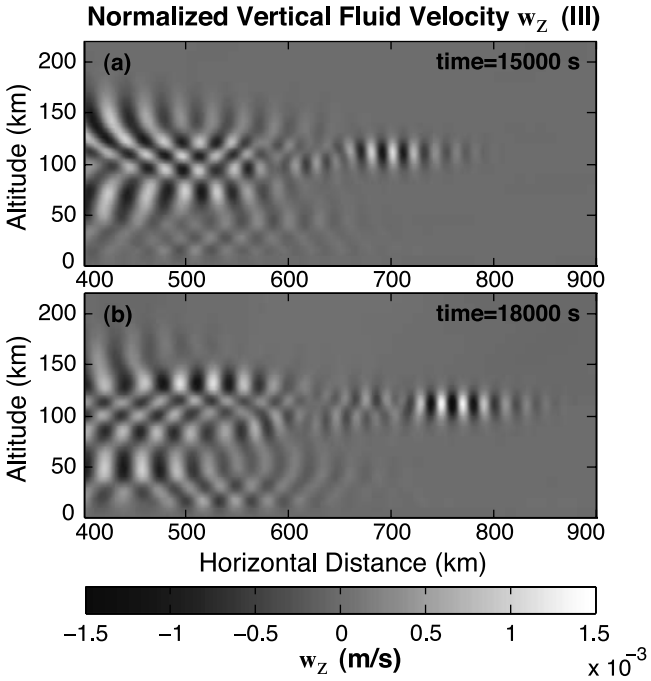

Figure 17. Normalized vertical perturbation velocity (normalized by density) plotted for two instants of time for case study III depicting (a) secondary wave propagation, phase velocity directed towards left and group velocity toward right, (b) secondary wave propagation after a later time step, showing group propagation away from original source location.

shows the primary wave as it propagates at 110 km altitude. Figure 19b shows the initiation of nonlinear wave energy transfer to the secondary harmonic wave as the primary wave propagates away from the duct. At the time step illustrated in Figure 19c (t = 10,500 s), both the primary and secondary waves are clearly visible. This progression in wave number is visible distinctly in the wave number spectra plotted in Figures 19d, 19e, and 19f. At later timesteps, after the primary wave has propagated away, the dominant feature is the secondary wave mode. The shape of the secondary wave spectrum is again consistent with that of the primary wave; the primary wave and secondary wave both strongly resemble the expected Gaussian-enveloped sinusoids. The interaction here is visibly simpler than in case study II, as the negative ground-relative group velocity allows the secondary wave to propagate away from the primary wave, preventing further nonlinear interactions.

[82] Figure 20 shows frequency spectral evolution for case study III in the center of the duct (~110 km altitude) at a point located 600 km from the left boundary of the domain. Similar to the horizontal wave number spectrum evolving in Figures 19d, 19e, and 19f, the initial Gaussian primary wave spectrum is visible strongly from t = 4000 to 6000 s. By t = 10,000 s, the secondary wave is strongly visible at this point at the predicted frequency.

6. Conclusions

[83] A fully nonlinear, two-dimensional, numerical model for the simulation of atmospheric gravity waves in a realistic background has been presented. This model has been used

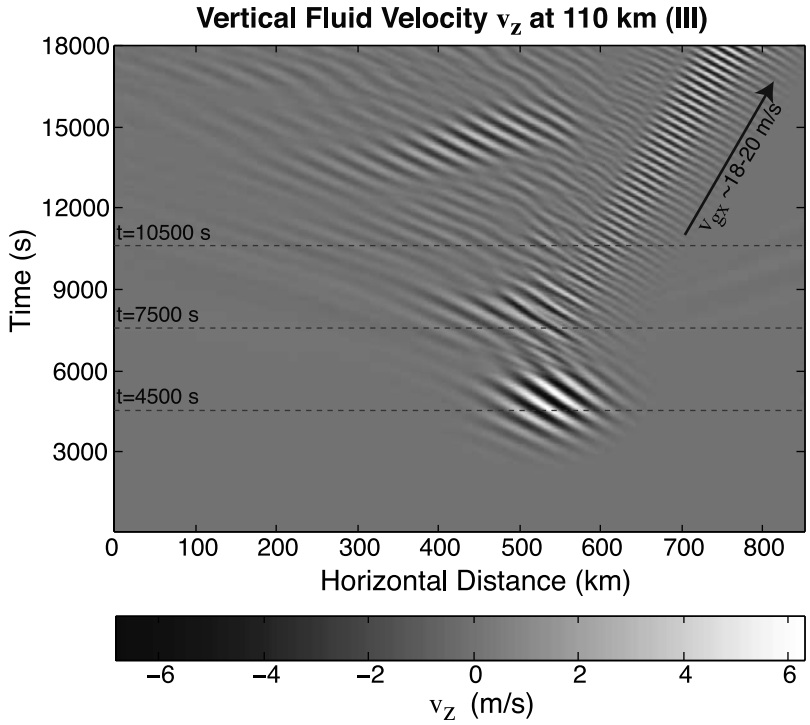

Figure 18. Time progression of vertical velocity taken at 110 km altitude and plotted over full duration of simulation run for breaking upstream excitation of harmonic secondary waves for case study III.

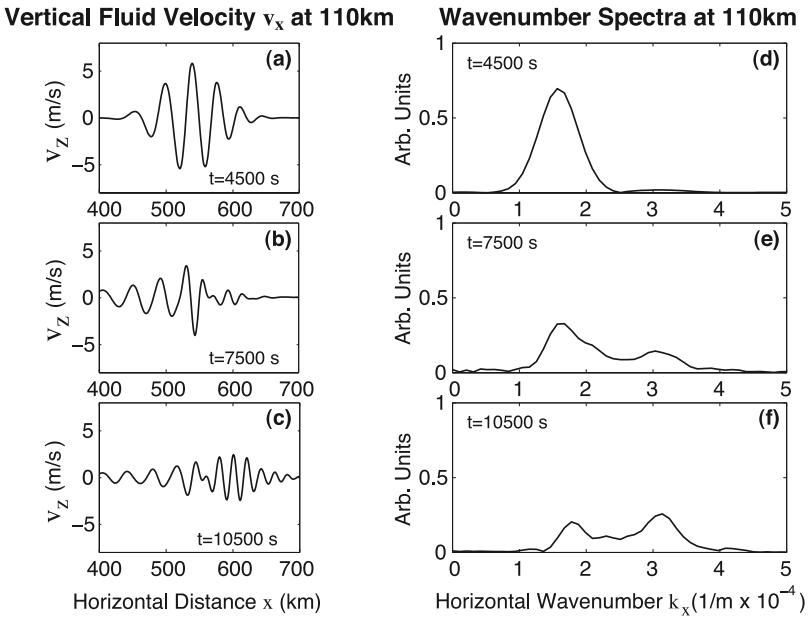

Figure 19. Vertical velocity line scans at 110 km (center of lower-thermospheric duct) for (a)t = 4500 s, (b) 7500 s, and (c) 10,500 s, respectively taken before, during, and after excitation of secondary waves for case study III. (d, e, f) Wave number spectra are illustrated, showing decrease of first harmonic intensity as the primary wave passes, and increase of second harmonic intensity as the secondary wave is excited.

in past studies [*Snively and Pasko*, 2003, 2005] for inviscid solutions. Results presented here include simple viscous and thermal-conductive background effects, leading to dissipation in both temperature/energy and momentum fields. The numerical model is based upon a flux-limited finite-volume method [*LeVeque*, 1997; *Bale et al.*, 2002], coupled with simple diffusion solvers and idealized gravity wave forcing. The model is stable for a wide range of physical conditions, supporting solutions for wave steepening and breaking with or without the application of physical molecular and eddy diffusion.

[84] Results presented for case study I demonstrate the linear excitation of a lower-thermospheric ducted wave via tunneling from a stratospheric duct and provide validation of numerical and analytical models. The presented results have been found consistent with past analytical [*Fritts and Yuan*, 1989] and numerical [*Walterscheid et al.*, 2001] studies. Simple wave tunneling is likely to be a significant linear source of propagating high-altitude ducted wave modes.

[85] Excitation of harmonic secondary waves by strong primary waves (breaking just above the duct) has been demonstrated for wave propagation along and against the direction of wind flow, in the presence of realistic molecular viscosity and thermal conduction. These results are consistent with results and predictions of *Chimonas et al.* [1996] and *Snively and Pasko* [2003], under quasi-realistic thermal conditions and constant wind flow.

[86] The variety of dynamic situations which facilitate nonlinear interactions suggest a possible link between the ~5 min ducted waves observed in the lower thermosphere and the ~10 min propagating waves typically generated by tropospheric sources. The observation of gravity waves propagating simultaneous to harmonic or near-harmonic waves in airglow measurements [e.g., *Smith et al.*, 2006] may indicate the occurrence of such nonlinear interactions.

[87] The magnitude of excited secondary waves is maximized for strong primary waves which break just above the duct. This is due to increased intensity of nonlinear interactions due to large magnitude, in addition to enhanced downward reflection of the primary wave packet by the destabilized region created by wavebreaking. Nonlinear resonant interactions near a breaking region have been reported by *Andreassen et al.* [1994] and *Franke and Robinson* [1999], where a breaking gravity wave was found to excite harmonic secondary waves even without the presence of an implicit thermal duct. Here, the nonperiodic domain and varying atmospheric thermal structure allow the secondary waves to be directly captured and to propagate away from the region of wave breaking. For the case study

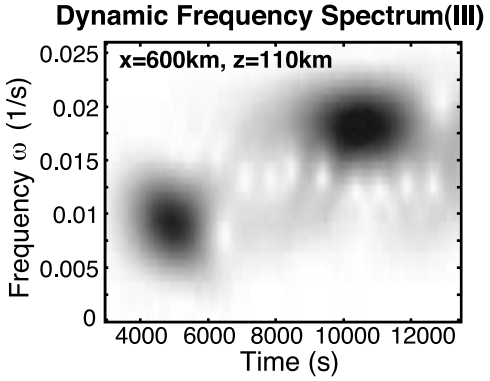

Figure 20. Dynamic frequency spectrum taken during the excitation of secondary waves by a breaking primary wave for case study III.

IIa, the total primary wave energy transferred nonlinearly to short period secondary waves is approaching 10%. This is likely higher than what could occur realistically, due to significant variability of the mesosphere and lower thermosphere. Future detailed modeling studies in self-consistent wind and thermal profiles are needed to assess the applicability and energetic significance of these interactions.

[88] For the case of wave propagation in the direction of wind flow (downwind), thermally ducted waves are shifted to lower intrinsic frequencies, resulting in ground-relative wave frequencies above the local Brunt-Väisälä frequency. This is consistent with wave events such as that reported by *Taylor et al.* [1995], where the ground-relative period was likely above the local Brunt-Väisälä frequency. For the case of wave propagation against the direction of wind flow (upwind), the intrinsic frequency of the ducted waves is shifted higher, resulting in trapping of waves which (when observed from the ground-relative reference frame) will appear to have periods too long for strong thermal ducting under windless conditions. When wind velocity within the duct exceeds the opposing intrinsic group velocity, the sum of the two becomes negative and the wave group propagates in the direction of wind flow, while the phase progresses against the wind flow. Results demonstrate that the constant wind does not preclude the nonlinear excitation of ducted waves by the processes examined, as long as local stability is not compromised. However, the propagation and directionality of the excited ducted waves will be strongly dependent on the local wind dynamics and structure, necessitating further investigation.

[89] **Acknowledgments.** This research was supported by NSF ATM-01-23020 and ATM-04-37140 grants to Pennsylvania State University.

[90] Amitava Bhattacharjee thanks David Fritts and another reviewer for their assistance in evaluating this paper.

References

Alexander, M. J., J. R. Holton, and D. R. Durran (1995), The gravity wave response above deep tropical convection in a squall line simulation, *J. Atmos. Sci.*, *52*(12), 2212–2226.

Andreassen, Ø., C. E. Wasberg, D. C. Fritts, and J. R. Isler (1994), Gravity wave breaking in two and three dimensions: 1. Model description and comparison of two-dimensional evolutions, *J. Geophys. Res.*, *99*(D4), 8095–8108.

Bale, D., R. J. LeVeque, S. Mitran, and J. A. Rossmanith (2002), A wave-propagation method for conservation laws and balance laws with spatially varying flux functions, *SIAM J. Sci. Comput.*, *24*, 955–978.

Brown, L. B., A. J. Gerrard, J. W. Meriwether, and J. J. Makela (2004), All-sky imaging observations of meospheric fronts in OI 557.7 nm and broadband OH airglow emissions: Analysis of frontal structure, atmospheric background conditions, and potential sourcing mechanisms, *J. Geophys. Res.*, *109*, D19104, doi:10.1029/2003JD004223.

Chimonas, G., and C. O. Hines (1986), Doppler ducting of atmospheric gravity waves, *J. Geophys. Res.*, *91*(D1), 1219–1230.

Chimonas, G., H. M. Hauser, and R. D. Bennett (1996), The excitation of ducted modes by passing internal waves, *Phys. Fluids*, *8*(6), 1486–1505.

Chung, J.-K., Y. H. Kim, and Y.-I. Won (2003), Observation of mesospheric waves with an all-sky camera in Korean Peninsula, *Adv. Space Res.*, *32*(5), 825–830.

Cummer, S. A. (2003), Dynamics of causal beam refraction in negative refractive index materials, *Appl. Phys. Lett.*, *82*(13), 2008–2009.

Dewan, E. M., and R. H. Picard (1998), Mesospheric bores, *J. Geophys. Res.*, *103*(D6), 6295–6305.

Dewan, E. M., R. H. Picard, R. R. O'Neil, H. A. Gardiner, J. Gibson, J. D. Mill, E. Richards, M. Kendra, and W. O. Gallery (1998), MSX satellite observations of thunderstorm-generated gravity waves in the mid-wave infrared images of the upper stratosphere, *Geophys. Res. Lett.*, *25*(7), 939–942.

Fovell, R., D. Durran, and J. R. Holton (1992), Numerical simulation of convectively generated stratospheric gravity waves, *J. Atmos. Sci.*, *49*(16), 1427–1443.

Franke, P. M., and W. A. Robinson (1999), Nonlinear behavior in the propagation of atmospheric gravity waves, *J. Atmos. Sci.*, *56*, 3010–3027.

Fritts, D. C., and M. J. Alexander (2003), Gravity wave dynamics and effects in the middle atmosphere, *Rev. Geophys.*, *41*(1), 1003, doi:10.1029/2001RG000106.

Fritts, D. C., and L. Yuan (1989), An analysis of gravity wave ducting in the atmosphere: Eckart's resonances in thermal and doppler ducts, *J. Geophys. Res.*, *94*(D15), 18,455–18,466.

Fritts, D. C., S. L. Vadas, K. Wan, and J. A. Werne (2006), Mean and variable forcing of the middle atmosphere by gravity waves, *J. Atmos. Sol. Terr. Phys.*, *68*, 247–265, doi:10.1016/j.jastp.2005.04.010.

Fukao, S., M. D. Yamanaka, N. Ao, W. K. Hocking, T. Sato, M. Yamamoto, T. Tsuda, and S. Kato (1994), Seasonal variability of vertical eddy diffusivity in the middle atmosphere: 1. Three-year observations by the m iddle and upper atmosphere radar, *J. Geophys. Res.*, *99*, 18,973–18,987.

Gossard, E. E., and W. H. Hooke (1975), *Waves in the Atmosphere*, Elsevier Sci., New York.

Groen, P. (1948), Contribution to the theory of internal waves, *Kon. Nederl. Meteorol. Inst. Mededel. Verh., Ser. B*, *2*(11), 23 pp.

Hecht, J. H., R. L. Walterscheid, M. P. Hickey, and S. J. Franke (2001), Climatology and modeliing of quasi-monochromatic atmospheric gravity waves observed over Urbana, Illinois, *J. Geophys. Res.*, *106*(D6), 5181–5195.

Hecht, J. M. (2004), Instability layers and airglow imaging, *Rev. Geophys.*, *42*, RG1001, doi:10.1029/2003RG000131.

Hedin, A. E. (1991), Extension of the MSIS thermospheric model into the middle and lower atmosphere, *J. Geophys. Res.*, *96*, 1159–1172.

Hines, C. O. (1960), Internal atmospheric gravity waves at ionospheric heights, *Can. J. Phys.*, *38*, 1441–1481.

Hines, C. O. (1974), *The Upper Atmosphere in Motion, Geophys. Monogr. Ser.*, 18, 1037 pp., AGU, Washington, D. C.

Hocking, W. K. (1990), Turbulence in the region 80–120 km, *Adv. Space Res.*, *10*(12), 153–161.

Horinouchi, T., T. Nakamura, and J. Kosaka (2002), Convectively generated mesoscale gravity waves simulated throughout the middle atmosphere, *Geophys. Res. Lett.*, *29*(21), 2007, doi:10.1029/2002GL016069.

Isler, J. R., M. J. Taylor, and D. C. Fritts (1997), Observational evidence of wave ducting and evanescence in the mesosphere, *J. Geophys. Res.*, *102*(D22), 26,301–26,313.

Jones, W. L. (1970), A theory for quasi-periodic oscillations observed in the ionosphere, *J. Atmos. Sci.*, *32*, 1555–1566.

Larsen, M. F., W. E. Swartz, and R. F. Woodman (1982), Gravity-wave generation by thunderstorms observed with a vertically-pointing 430 MHz radar, *Geophys. Res. Lett.*, *9*(5), 571–574.

LeVeque, R. J. (1997), Wave propagation algorithms for multidimensional hyperbolic systems, *J. Comput. Phys.*, *131*, 327–353.

LeVeque, R. J. (2002), *Finite Volume Methods for Hyperbolic Problems*, Cambridge Univ. Press, New York.

Mayr, H. G., I. Harris, F. A. Herrero, and F. Varosi (1984), Global excitation of wave phenomena in a multiconstituent medium. I – Transfer function of the Earth's thermosphere. II – Impulsive perturbations in the Earth's thermosphere, *J. Geophys. Res.*, *89*, 10,929–10,986.

Munasinghe, G., H. Hur, Y. T. Huang, A. Bhattachryya, and T. F. Tuan (1998), Application of the dispersion formula to long- and short-period gravity waves: Comparisions with ALOHA-93 data and analytical model, *J. Geophys. Res.*, *103*(D6), 6467–6481.

Nakamura, T., A. Higashikawa, T. Tsuda, and Y. Matsushita (1999), Seasonal variations of gravity wave structures in OH airglow with a CCD imager at Shigaraki, *Earth Planets Space*, *51*, 897–906.

Piani, C., D. Durran, M. J. Alexander, and J. R. Holton (2000), A numerical study of three-dimensional gravity waves triggered by deep tropical convection and their role in the dynamics of the QBO, *J. Atmos. Sci.*, *57*(22), 3689–3702.

Pierce, A. D., and S. C. Coroniti (1966), A mechanism for the generation of acoustic-gravity waves during thunderstorm formation, *Nature*, *210*(5042), 1209–1210.

Roe, P. L. (1981), Approximate Riemann solvers, parameter vectors, and fiference schemes, *J. Comput. Phys.*, *43*, 357–372.

Satomura, T., and K. Sato (1999), Secondary generation of gravity waves associated with the breaking of mountain waves, *J. Atmos. Sci.*, *56*, 3847–3858.

Sentman, D. D., et al. (2003), Simultaneous observations of mesospheric gravity waves and sprites generated by a midwestern thunderstorm, *J. Atmos. Sol. Terr. Phys.*, *65*, 537–550.

Seyler, C. E. (2005), Internal waves and undular bores in mesospheric inversion layers, *J. Geophys. Res.*, *110*, D09S05, doi:10.1029/2004JD004685.
Smith, S. M., M. J. Taylor, G. R. Swenson, C. Y. She, W. K. Hocking, J. Baumgardner, and M. Mendillo (2003), A multidiagnostic investigation of the mesospheric bore phenomena, *J. Geophys. Res.*, *108*(A2), 1083, doi:10.1029/2002JA009500.
Smith, S. M., J. P. Friedman, S. Raizada, C. Tepley, J. Baumgardner, and M. Mendillo (2005), Evidence of mesospheric bore formation from a breaking gravity wave event: Simultaneous imaging and lidar measurements, *J. Atmos. Sol. Terr. Phys.*, *67*(4), doi:10.1016/j.jastp.2004.11.008.
Smith, S. M., J. Scheer, E. R. Reisen, and J. Baumgardner (2006), Characterization of exceptionally strong mesospheric wave events using all-sky and zenith airglow observations, *J. Geophys. Res.*, *111*, A09309, doi:10.1029/2005JA011197.
Snively, J. B., and V. P. Pasko (2003), Breaking of thunderstorm-generated gravity waves as a source of short-period ducted waves at mesopause altitudes, *Geophys. Res. Lett.*, *30*(24), 2254, doi:10.1029/2003GL018436.
Snively, J. B., and V. P. Pasko (2005), Antiphase OH and OI airglow emissions induced by a short-period ducted gravity wave, *Geophys. Res. Lett.*, *32*, L08808, doi:10.1029/2004GL022221.
Snively, J. B., V. P. Pasko, M. J. Taylor, and W. K. Hocking (2007), Doppler ducting of short-period gravity waves by midlatitude tidal wind structure, *J. Geophys. Res.*, *113*, A03304, doi:10.1029/2006JA011895.
Stull, R. B. (1976), Internal gravity waves generated by penetrative convection, *J. Atmos. Sci.*, *33*, 1279–1286.
Sutherland, B. R., and K. Yewchuk (2004), Internal wave tunnelling, *J. Fluid Mech.*, *511*, 125–134.
Taylor, L. L. (1979), Mesospheric heating due to intense tropical convection, *NASA Contractor Rep. 3132*, NASA, Washington, D. C.
Taylor, M. J., and R. Edwards (1991), Observations of short period mesospheric wave patterns: In situ or tropospheric wave generation?, *Geophys. Res. Lett.*, *28*(7), 1337–1340.
Taylor, M. J., and H. A. Hapgood (1988), Identification of a thunderstorm as a source of short period gravity waves in the upper atmospheric nightglow emissions, *Planet. Space Sci.*, *36*, 975–985.
Taylor, M. J., D. N. Turnbull, and R. P. Lowe (1995), Spectrometric and imaging measurements of a spectacular gravity wave event observed during the ALOHA-93 campaign, *Geophys. Res. Lett.*, *22*(20), 2849–2852.
Thorpe, S. A. (1968), On the shape of progressive internal waves, *Phil. Trans. R. Soc. London, Ser. A*, *263*, 563–614.
Vadas, S. L., D. C. Fritts, and M. J. Alexander (2003), Mechanism for the generation of secondary waves in wave breaking regions, *J. Atmos. Sci.*, *60*, 194–214.
Veselago, V. G. (1968), The electrodynamics of substances with simultaneously negative values of ϵ and μ, *Sov. Phys. Usp.*, *10*(4), 509–514.
Walterscheid, R. L., and G. Schubert (1990), Nonlinear evolution of an upward propagating gravity wave: Overturning, convection, transience and turbulence, *J. Atmos. Sci.*, *47*(1), 101–125.
Walterscheid, R. L., J. H. Hecht, R. A. Vincent, I. M. Reid, J. Woithe, and M. P. Hickey (1999), Analysis and interpretation of airglow and radar observations of quasi-monochromatic gravity waves in the upper mesosphere and lower thermosphere over Adelaide, Australia, *J. Atmos. Sol. Terr. Phys.*, *61*, 461–478.
Walterscheid, R. L., G. Schubert, and D. G. Brinkman (2001), Small-scale gravity waves in the upper mesosphere and lower thermosphere generated by deep tropical convection, *J. Geophys. Res.*, *106*(D23), 31,825–31,832.
Yu, Y., and M. P. Hickey (2007), Time-resolved ducting of atmospheric acoustic gravity waves by analysis of the vertical energy flux, *Geophys. Res. Lett.*, *34*, L02821, doi:10.1029/2006GL028299.
Zhou, X., J. R. Holton, and G. L. Mullendore (2002), Forcing of secondary waves by breaking of gravity waves in the mesosphere, *J. Geophys. Res.*, *107*(D7), 4058, doi:10.1029/2001JD001204.

V. P. Pasko, CSSL Laboratory, Department of Electrical Engineering, Pennsylvania State University, 211B Electrical Engineering East, University Park, PA 16802, USA. (vpasko@psu.edu)

J. B. Snively, Center for Atmospheric and Space Sciences, Utah State University, SER Building, Logan, UT 84322, USA. (jonathan.snively@usu.edu)